

Ni- and Co-struvites: Revealing crystallization mechanisms and crystal engineering for phosphorous and transition metal recovery

Stephanos Karafiludis^{1*}, Ana Guilherme Buzanich¹, Zdravko Kochovski², Ines Feldmann¹, Franziska Emmerling^{1,3}, and Tomasz M. Stawski^{1**}

¹Federal Institute for Materials Research and Testing, Richard-Willstätter-Straße 11, 12489 Berlin, Germany

²Department for Electrochemical Energy Storage, Helmholtz-Zentrum Berlin for Materials and Energy, Hahn-Meitner Platz 1, 14109 Berlin, Germany

³Department of Chemistry, Humboldt-Universität zu Berlin, Brook-Taylor-Straße 2, 12489 Berlin

Stephanos Karafiludis: <https://orcid.org/0000-0002-7257-6311>;

Ana Guilherme Buzanich: <https://orcid.org/0000-0001-5543-9924>;

Zdravko Kochovski: <https://orcid.org/0000-0001-8375-0365> ;

Ines Feldmann: <https://orcid.org/0000-0003-2650-9270> ;

Franziska Emmerling: <https://orcid.org/0000-0001-8528-0301>;

Tomasz M. Stawski: <https://orcid.org/0000-0002-0881-5808>;

Corresponding authors: **tomasz.stawski@bam.de; *stephanos.karafiludis@bam.de

Keywords: struvite; nickel; cobalt; phosphate; phosphorous recovery; crystallization

Synopsis

We studied crystallization of Ni- and Co-struvites to simultaneously recover environmental harmful phosphate, ammonium and toxic transition metal cations from wastewaters.

Abstract

Wastewaters containing high concentrations of NH_4^+ , PO_4^{3-} and transition metals are environmentally harmful and toxic pollutants. At the same time phosphorous and transition metals constitute valuable resources. Typically, separate pathways have been considered to extract hazardous transition metals or phosphate, independently from each other. Investigations on the simultaneous removal of multiple components have been studied only to a limited extent. Here, we report the synthesis routes for Co- and Ni-struvites ($\text{NH}_4\text{MPO}_4 \cdot 6\text{H}_2\text{O}$, $\text{M} = \text{Ni}^{2+}$, Co^{2+}), which allow for P, ammonia and metal co-precipitation. By evaluating different reaction parameters, which are representative for some common wastewater compositions, the phase and stability of transition metal struvites, as well as their crystal morphologies, and sizes could be optimized. Ni-struvite is stable in a wide reactant concentration range and at different metal/phosphorus (M/P) ratios, whereas Co-struvite only forms at low M/P ratios. Detailed investigations of the precipitation process using ex situ and in situ techniques provided insights in the crystallization mechanisms. Ni- and Co-struvites crystallize via intermediate colloidal nanophases which subsequently aggregate and condense to final crystals after extended reaction times. This mechanism is different from the practically immediate crystallization of micrometer-sized crystals of ordinary struvite ($\text{NH}_4\text{MgPO}_4 \cdot 6\text{H}_2\text{O}$), which does not seem to involve any amorphous precursor phase. The achieved level of control over the morphology and size, makes precipitation of transition metal struvites a promising method for wastewater treatment. The crystals can be potentially upcycled into precursor raw materials e.g. for electrochemical or (electro)catalytical applications.

Introduction

Recovery and recycling of critical and essential elements has crucial importance for maintaining of sustainable use of raw materials. Phosphorus is an important, yet, limited natural resource. It is widely used in modern agriculture, mainly in fertilizers, but this element is not fully recyclable. In the mid-term future it could be potentially depleted as a raw material due to the high demand and rapidly declining natural phosphorite ore deposits ^{1, 2}. Thus, phosphate rocks are included in the European Union's list of critical raw materials (CRMs) ³. At the same time, due to the incomplete P-cycle in nature ⁴, phosphorous also causes major problems to the environment such as eutrophication of aquatic systems and is effectively lost for use. Therefore, due to simultaneous scarcity and abundance, the phosphorus recovery from agricultural, industrial, mining, or urban wastewaters have been an important factor in sustaining our global consumption and preservation of the natural environment.

In general terms, phosphorous recovery relies on precipitation of P-bearing mineral phases ^{5, 6}. Therefore, phosphorous recovery cannot be conducted without considering the presence and the "co-recovery" of metal counter-ions. Alkaline earth metals are ubiquitous, and as such are neither of any particular interest, nor do constitute an environmental risk. In contrast, many d-block-elements are likely pollutants and/or valuable resources. These factors are especially important in the case of the controlled precipitation/crystallization of struvite from wastewater which is already a promising P-recovery route ^{7, 8}. Struvite is $\text{NH}_4\text{MPO}_4 \cdot 6\text{H}_2\text{O}$, where M^{2+} is usually Mg^{2+} , but other divalent cations such as Ni^{2+} , Co^{2+} , Zn^{2+} , Cu^{2+} can potentially substitute Mg^{2+} in the struvite structure due to similar ionic radii ^{7, 9-11}. These recovered M-struvites, with $\text{M} = \text{Ni}$ and/or Co , could act as storage materials for transition metals that may be potentially up-cycled for industrial applications as raw materials for transition metal phosphate (electro)catalysts ¹²⁻¹⁵. While the synthesis of Mg-struvite is sufficiently understood ^{8, 16} and used in practice ¹⁷, investigations of crystallization of transition metal struvites are scarce. Most of these studies focus on the incorporation of transition metals ¹⁸⁻²¹ or other components ²² majorly through adsorption rather than the complete substitution of magnesium in the struvite structure ^{18, 23-25}. Although, transition metal struvites share their fundamental crystal structure with Mg-struvite, their crystallization pathways, growth kinetics, thermodynamic stability or transformations differ among each other and from for the parent compound, Mg-struvite ^{26, 27}. In transition metal phosphate recovery routes aimed at potential up-cycling, the holistic approach towards the crystallization routes is crucial. The goal is to obtain a given phase, but it should also exhibit engineered or at least predictable properties such as crystal size, shape, aspect ratio etc. Such crystal engineering of a desired chemical compound determines its performance and scalability in industrial applications. Thus, firstly the optimized reaction conditions lead to efficient M-struvite precipitation, and therefore to significantly improved phosphorous, Ni, and Co recovery out of wastewaters. Secondly, such "engineered" M-struvite crystals may be further directly used as tailor-made upcycled precursor materials for specific applications e.g. in (electro)catalysis ^{14, 15, 22, 28}.

Here, we present the effect of physicochemical conditions of aqueous solutions onto the precipitation of Ni- and Co-struvites. The chosen conditions closely match those typical for

several wastewater compositions. Our findings are compared with the parent Mg-struvite. We highlight the systematic differences in crystallization pathways of Ni- and Co-struvite at all stages, where the stability and speciation of the precursor phases is linked to the overall evolution of struvite crystals.

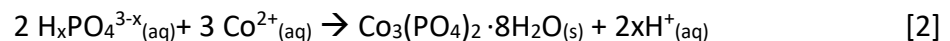
Methods

Synthesis

(NH₄)₂HPO₄ (DAP) (ChemSolute, 99%), MgCl₂·6H₂O, NiSO₄·6H₂O (ChemSolute, 99%) and CoSO₄·7H₂O (Alfa Aesar, 98 %) were used to synthesize metal phosphates under different reaction conditions from 0.004-0.3 M for NiSO₄, CoSO₄ and MgCl₂ and 0.02-0.1 mM for DAP. All detailed reaction conditions are listed in the SI (SI: Table S1). Our work was primarily focused on Ni and Co, but for the sake of comparison we are also synthesized and investigated common struvite (NH₄MgPO₄·6H₂O) at several selected concentrations (SI: Table S2). Based on the above-mentioned concentrations we used the metal-to-phosphate ratios (M/P) ranging for Ni and Mg from 0.02 to 3, and for Co from 0.01 to 3 to characterize each sample. At first 1 M stock solutions of DAP and the metal salts were prepared. The aqueous solutions were made by dissolving the calculated amount of salt in double ionized water (> 18 MΩ·cm). In a simple “one pot” approach, typically 100 ml of DAP and 100 ml of metal-bearing solution were mixed on a magnetic stirrer (300 rpm) at room temperature (25°C). The precipitation reaction of M-struvite was occurring according to the following mass-balance equation (eq. [1]):



Eq. [1] was in general valid for Ni regardless of the metal concentration used, as well as for Co at lower concentrations below a M/P ratio of 0.4. However, at high concentrations of Co²⁺ above a M/P ratio of 0.4 we observed the crystallization of cobalt(II)phosphate octahydrate (CPO) instead of Co-struvite (COS) according to eq. [2]:



To evaluate how the pH influences the crystal morphology, size and stability of M-struvites, sample series of Ni, Co and Mg were synthesized at different initial pH values by adding varying amounts (1-10 ml) of 1 M NaOH_(aq) or 0.1 M H₂SO_{4(aq)}. Here, we used $c(\text{M}^{2+}) = 0.02 \text{ M}$ and $c(\text{DAP}) = 0.1 \text{ M}$ to remain for all chemical systems (Ni, Co and Mg) within the phase stability field of M-struvite. For further analysis, the solid phases precipitated from the mixed solutions were collected onto a cellulose filter (pore size 1 μm, LABSOLUTE) by using a vacuum filtration kit (i.e. Büchner funnel). Afterwards the powders were left to dry in air at room temperature for 2 hours.

Thermodynamic calculations

All reaction conditions were, prior to the experiments, evaluated and verified by calculations with the aqueous geochemical simulation program PHREEQC²⁹ using the Lawrence Livermore National Library database (llnl.dat). Missing entries about transition metal struvites in the database were completed with data from Madsen *et. al.* 2017³⁰.

pH measurements

The reaction progress was followed in situ by measuring pH as protons were released during precipitation (see eq.[1] and [2]). The pH was continuously measured with a pH electrode connected to a data logger board “DrDAQ” time resolution of 1 s (Pico Technology, Cambridgeshire, UK).

X-ray diffraction

Powder X-ray diffraction (PXRD, XRD) data from the precipitated powders were collected on a D8 Bruker Diffractometer equipped with a LYNXEYE XE-T detector. Diffraction was measured with Cu K α radiation (1.5406 Å, 40 kV and 40 mA) from 5-60° using a step size 0.015° (2 Θ) and a scanning time of 0.5 s per step.

SEM

The scanning electron microscopy (SEM) characterization was conducted on an FEI XL 30 tungsten cathode scanning electron microscope operated at 20 keV and using a secondary electron detector. Prior to the analysis all samples were coated with a 30 nm thick layer of gold.

Dry-TEM

Dry (i.e. particles directly exposed to high vacuum) transmission electron microscopy (TEM) images were obtained on a Talos F200S Microscope (Thermo Fisher Scientific) operating at 200 kV. A Ceta 16M camera (TEM mode) and a HAADF (high-angle annular dark field) detector (STEM mode; Scanning Transmission electron microscopy) were used to capture the images. Additionally, to collect detailed elemental information, energy dispersive X-ray spectroscopy (EDS) was performed by two side-entry retractable silicon drift detectors (SDD). A counting time of 60 s was applied for point measurements while for the elemental maps 40-50 frames were taken resulting in a counting time of 1 hour. The specimen was prepared by mixing the 100 μ l of reactant solutions in an Eppendorf tube (1.5 ml) for 5 seconds of reaction time and dropping 10 μ l of the sample solution onto a 3 mm holey carbon-coated Cu-grid (Lacey Carbon, 400 mesh). Then, the specimens were left to dry at room temperature for 5 minutes.

Cryo-TEM

Under “dry” conditions, due to beam damage and high-vacuum, precipitated phases may develop mesopores similar to what is observed in crystalline struvite after thermal treatment²⁷. Cryo-TEM allowed us to prevent beam damage artefacts of the material. Cryo-EM imaging was performed with a JEOL JEM-2100 transmission electron microscope (JEOL GmbH, Eching, Germany). Specimens were prepared by casting a 4 μ l droplet of sample solution onto lacey carbon-coated copper TEM grids (200 mesh, Electron Microscopy Sciences, Hatfield, PA) and plunge-freezing them into liquid ethane using an FEI vitrobot Mark IV set at 4°C and 95% humidity. Vitrified grids were either transferred directly to the microscope’s cryo-transfer holder (Gatan 914, Gatan, Munich, Germany) or stored in liquid nitrogen. All grids were glow-

discharged before use. Imaging was carried out at temperatures around -180°C . The TEM was operated at an acceleration voltage of 200 kV, and an objective lens defocus of about $1.5\text{--}2\ \mu\text{m}$ was used to increase the contrast. Micrographs were recorded with a bottom-mounted 4.4k CMOS camera (TemCam-F416, TVIPS, Gauting, Germany). The total electron dose in each micrograph was kept below $20\ e^{-}/\text{\AA}^2$.

X-ray Absorption Spectroscopy (XAS)

To evaluate and compare the metal coordination environments in different phases obtained through synthesis, XANES (near-edge X-ray absorption fine structure) and EXAFS (extended X-ray absorption fine-structure) spectroscopy measurements were performed at the BAMline (BESSY-II, Helmholtz Centre Berlin for Materials and Energy Berlin, Germany) ³¹.

The beam was monochromatized using a silicon double-crystal monochromator (DCM) with a crystallographic orientation of [111]. The size of the beam was 3 mm (l) x 1 mm (h). The measurements were performed at Co-K edge (7709 eV) and Ni-K edge (8333 eV) in transmission geometry, with two ionization chambers as detectors. The excitation energy was varied from 7606 eV to 8678 eV for Co and 8230 eV to 9302 eV for Ni, with varying energy steps. For the pre-edge region, the energy was varied in 10 eV steps; for the region around the edge, energy was tuned first in 0.5 eV steps, then in 1 eV steps and in the EXAFS region with a constant step in the k-space of $0.04\ \text{\AA}^{-1}$. The associated uncertainties were experimentally determined by measuring the cobalt and nickel metal foils, each 10 times. A value of $\pm 0.3\ \text{eV}$ was obtained for both systems. For the measurement, the samples were mixed with boron nitride, placed in polycarbonate hole plates with a thickness of 1 mm and sealed with a polyimide tape (Kapton) on both sides. Before collecting the sample spectra, a cobalt or nickel foil was used as a reference for the respective K edges. The relative energies of the spectra were calibrated to the first inflection point from the first derivative of the cobalt/nickel metal absorption edge.

The resulting EXAFS data were processed by using ATHENA and ARTEMIS. Both programs belong to the main package IFEFFIT (v. 1.2.11) ³². All crystallographic structures were visualized with VESTA (v. 3.5) ³³.

Results

The synthesis of transition metal struvites was optimized using different reaction conditions (SI: Tables S1 and S2). The concentrations of the reactant solutions (Mg^{2+} , Ni^{2+} and Co^{2+}) and initial pH values were varied to explore the phase stability field. Concentrations were chosen to be representative for several wastewater types (SI: Table S3 and Supplementary Note 1).

Phase composition in the transition metal phosphate systems

We explored the potential phase diagrams in the transition metal/DAP systems of M-struvites, $M = \text{Mg}, \text{Ni}$ and Co (SI: Figure S1). The data points are derived from the XRD measurements (SI: Figure S2 and S3). At all concentration of Mg^{2+} , Ni^{2+} and for all the different M/P ratios, pure single-phase Mg or Ni-struvites ($\text{NH}_4\text{MgPO}_4 \cdot 6\text{H}_2\text{O}$, $\text{NH}_4\text{NiPO}_4 \cdot 6\text{H}_2\text{O}$) are present (SI: Figure S1A-C). In the Co system at high DAP concentrations of 0.1 M only at a low M/P < 0.4 , Co-struvite $\text{NH}_4\text{CoPO}_4 \cdot 6\text{H}_2\text{O}$ (COS) precipitated as a pure single phase (SI: Figure S1D). At higher M/P > 0.5 , cobalt(II)phosphate octahydrate $\text{Co}_3(\text{PO}_4)_2 \cdot 8\text{H}_2\text{O}$ (CPO) is formed as the only phase. In the intermediate interval $0.5 > \text{M/P} > 0.4$ a binary mixture of CPO and COS is formed (SI: Figure S3A). At lower concentrations of DAP of 0.02 M the transition M/P ratio of Co-struvite to Co-octahydrate is slightly reduced toward lower values < 0.4 .

To evaluate how the initial pH impacts the phase stability of M-struvites, different amounts 1-10 ml of 1 M $\text{NaOH}_{(\text{aq})}$ and 0.1 M $\text{H}_2\text{SO}_{4(\text{aq})}$ were added prior to mixing. For all the samples in a pH-series, $c(\text{M}^{2+}) = 0.02 \text{ M}$ and $c(\text{DAP}) = 0.1 \text{ M}$ were used to ensure, that the crystals formed within the phase stability field of M-struvite, common for all the systems ($M = \text{Mg}^{2+}, \text{Ni}^{2+}, \text{Co}^{2+}$). Indeed, for all initial pH adjusted samples and independent of the metal used, M-struvites formed as pure single phase (SI: Figure S4A-F). We calculated the final equilibrium state of the solution based on the calculations with PHREEQC (SI: Table S2).

Evolution of precipitation reaction and the role of transitional colloidal phases

In both Ni and Mg systems the respective M-struvite formed as a pure single phase regardless of the reactant concentrations (SI: Figure S1). However, in the case of Co at concentrations of $c(\text{Co}^{2+}) > 0.4 \text{ M}$ with $c(\text{DAP}) = 0.1 \text{ M}$ other phases precipitated. The phase diagrams (SI: Figure S1) reflect only the final close-to-equilibrium outcome of the crystallization experiments. However, it must be further appended by the observations we made during our studies, which hint about the pathways by which the phases formed. The Co-struvite samples spontaneously dehydrated in air to Co-dittmarite $\text{NH}_4\text{CoPO}_4 \cdot \text{H}_2\text{O}$ (COD), as it was evidenced by the XRD (ambient lab conditions, 1 to 3 days depending on a concentration 0.004 M ($t = 1 \text{ d}$) to 0.4 M ($t = 3 \text{ d}$)) and was indicated by a color change from light purple to light pink. After several minutes the cobalt phosphate phases transformed from amorphous into crystalline which was accompanied by a color change from blue, to purple, to light pink (SI: inset in Figure S1D). The time after which the transformation occurred, was highly dependent on the stirring rate, temperature, pH, and concentration of the reactants^{26, 34, 35}. In the Ni-struvite system, we also observed a very short-lived apparent colloidal precursor phase, as was hinted by a smooth color transition from light green to emerald. On the other hand, in Mg-struvite such early-

stage transformations were not apparent within the observational window. These indicated complex crystallization pathways of transition metal struvite should be studied more from point of their evolution rather than their final products.

Therefore, in order to establish the sequence of distinct stages during the evolution of potential struvites, we followed the crystallization mechanisms by conducting time-resolved pH measurements. The evolution of pH constituted a proxy for reaction progress, following eqs. [1] and [2]. Consequently, we measured pH vs. time for different metal concentrations M^{2+} for up to 3600 s (SI: Figure S5, Supplementary Note 2). Based on those relatively simple in situ measurements, we found that the transitional metal systems differ significantly from the Mg system for all the concentration runs. The as-observed pH trends and the accompanying color changes of the solution are likely to indicate the presence of long- to short-lived colloidal phases in the transition metal systems on the way to final crystal (Figure S5, Supplementary Note 2). Therefore, as these transitional phases^{26, 35-38} affect both the kinetics of the precipitation reaction as well as crystallinity of the final products, it was necessary to investigate them at least at the early stages of nucleation. For this purpose, ex situ dry TEM and cryo-TEM measurements combined with EDS mappings and SAED analysis were performed. Each sample was prepared for a reaction time of 5 seconds (Figure 1), as was established based on the pH measurements. The Mg sample showed μm -sized crystals of needle-shaped Mg-struvite with well-developed planes (Figure 1A and SI: Figure S6). In contrast, the Ni- and Co-samples exhibited amorphous (see SAEDs in Figure 1) round nanoparticles with sizes of ~ 50 nm and chemical composition very close to M-struvite, which agglomerated to bigger units (Figure 1B-D, SI: Figures S7 and S8). The Ni-nanoparticles and their aggregates appeared more condensed and regular compared to those of Co. Based on the pH trends (SI: Figure S5) it was apparent that the Ni system contained short-lived nanophases present for several seconds, while for the Co system the nanophases were relatively long-lived and stable up to hours.

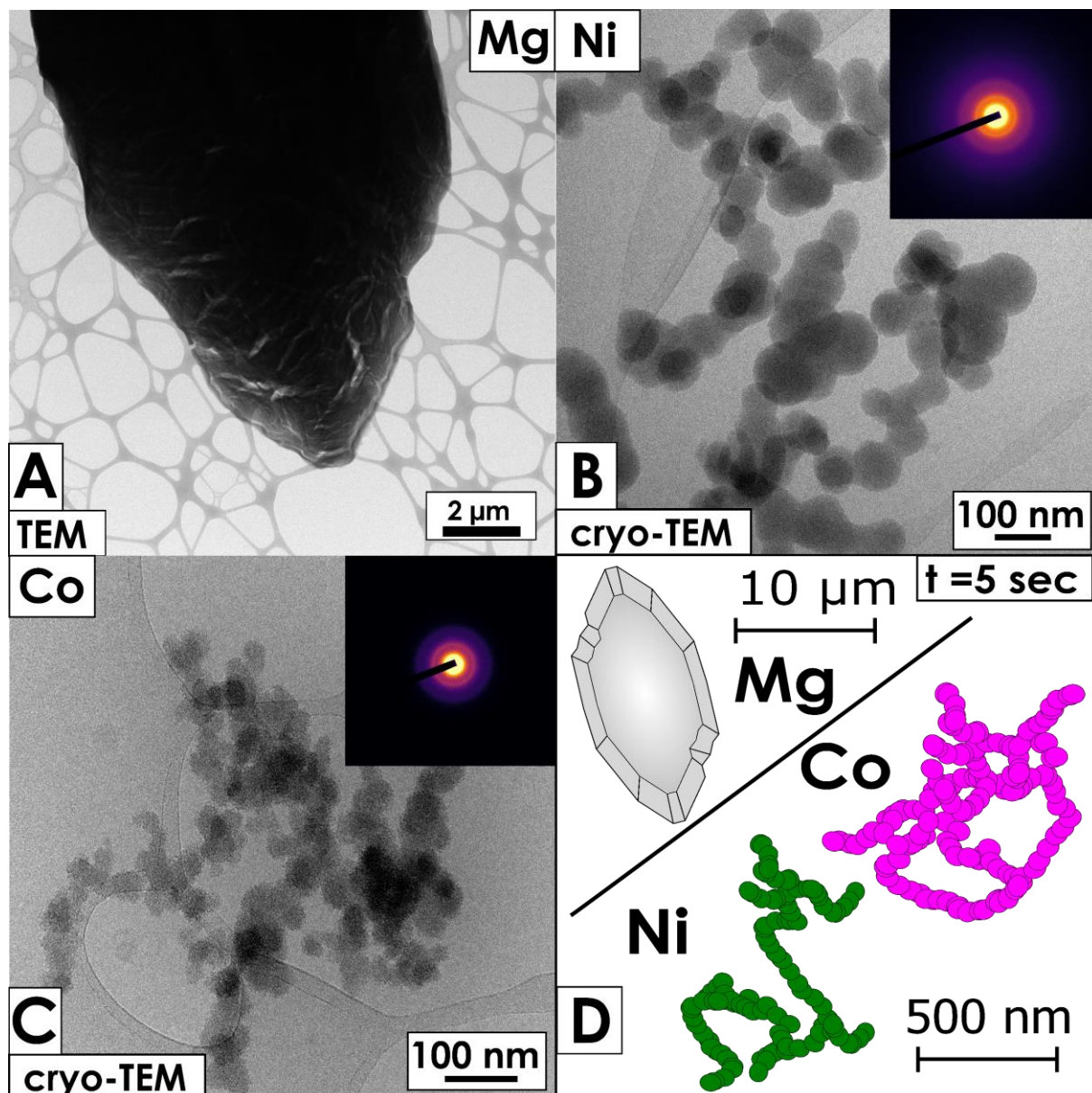


Figure 1: (A) Dry TEM image of a Mg-struvite crystal after 5 seconds of mixing ; (B) cryo-TEM images of Ni sample after 5 seconds mixing with an inset of the SAED pattern; (C) cryo-TEM images of Co sample after 5 seconds mixing with an inset of the SAED pattern; (D) a network of sphere-shaped particles are clearly amorphous; summarizing sketch of the observed features; supporting detailed STEM images, EDS mappings and point measurements can be found in the SI (SI: Figures S6-S8); The SAED patterns clearly show that the imaged particles were amorphous.

Crystal engineering of transition metal phosphates

To quantify how the changes in concentration of transition metal M^{2+} and DAP, as well as the initial pH, affect the morphology and size of the crystallites, SEM analysis was performed on crystals synthesized for various conditions (Figure 2). A strong dependency of the morphology and size of the crystals was observed in the Ni-system in respect to the M/P ratio (Figure 2A, SI: Figure S9). Ni-struvite morphologies with an M/P ratio ≥ 1 (high $c(Ni^{2+})$ compared to low $c(DAP)$) showed an anhedral rounded appearance and numerous agglomerated crystal nuclei with a crystallite size of $11 \pm 3 \mu m$ (length from edge-to-edge) at $c(Ni) = c(DAP) = 100 \text{ mM}$. At low M/P ratios ≤ 1 (low $c(Ni^{2+})$ compared to high $c(DAP)$) the crystals exhibited a more euhedral

elongated X- or “coffin-like” shaped habit with crystallite size of $55 \pm 9 \mu\text{m}$ at $c(\text{Ni}) = 20 \text{ mM}$ and $c(\text{DAP}) = 100 \text{ mM}$. The X-shaped habit of the crystals occurred at low M/P ratios < 0.5 and high $c(\text{DAP}) \geq 50 \text{ mM}$ while the “coffin-like” morphology appeared at low M/P ratios < 0.5 , but at low $c(\text{DAP}) \leq 50 \text{ mM}$. High Ni^{2+} concentrations at a constant DAP concentration favored numerous crystallites of smaller size with an anhedral appearance, while high DAP concentrations at a constant Ni^{2+} concentration led to an increase in the crystallite size and idiomorphism of the crystallites. Adding $\text{NaOH}_{(\text{aq})}$ and the coupled increase of pH favored the formation of M-struvite due to the fact that protons were released through the precipitation reaction which counteracted the pH effect of OH^- ions (eq.[1]) while adding $\text{H}_2\text{SO}_{4(\text{aq})}$ inhibited the precipitation. Adding $\text{NaOH}_{(\text{aq})}$ to the Ni-struvite system alter the crystal morphology strongly and decreased the crystallite size from $50 \pm 9 \mu\text{m}$ to $5 \pm 1 \mu\text{m}$ (grey inset in Figure 2A, SI: Figure S10). In addition, it changed the crystal habit to an orthorhombic prism appearance. Adding $\text{H}_2\text{SO}_{4(\text{aq})}$ affected the surface of the crystals strongly, although under these conditions the crystallite size and the X-shaped-like morphology were not influenced in comparison with the pH-unadjusted sample at the same M^{2+} and DAP concentrations.

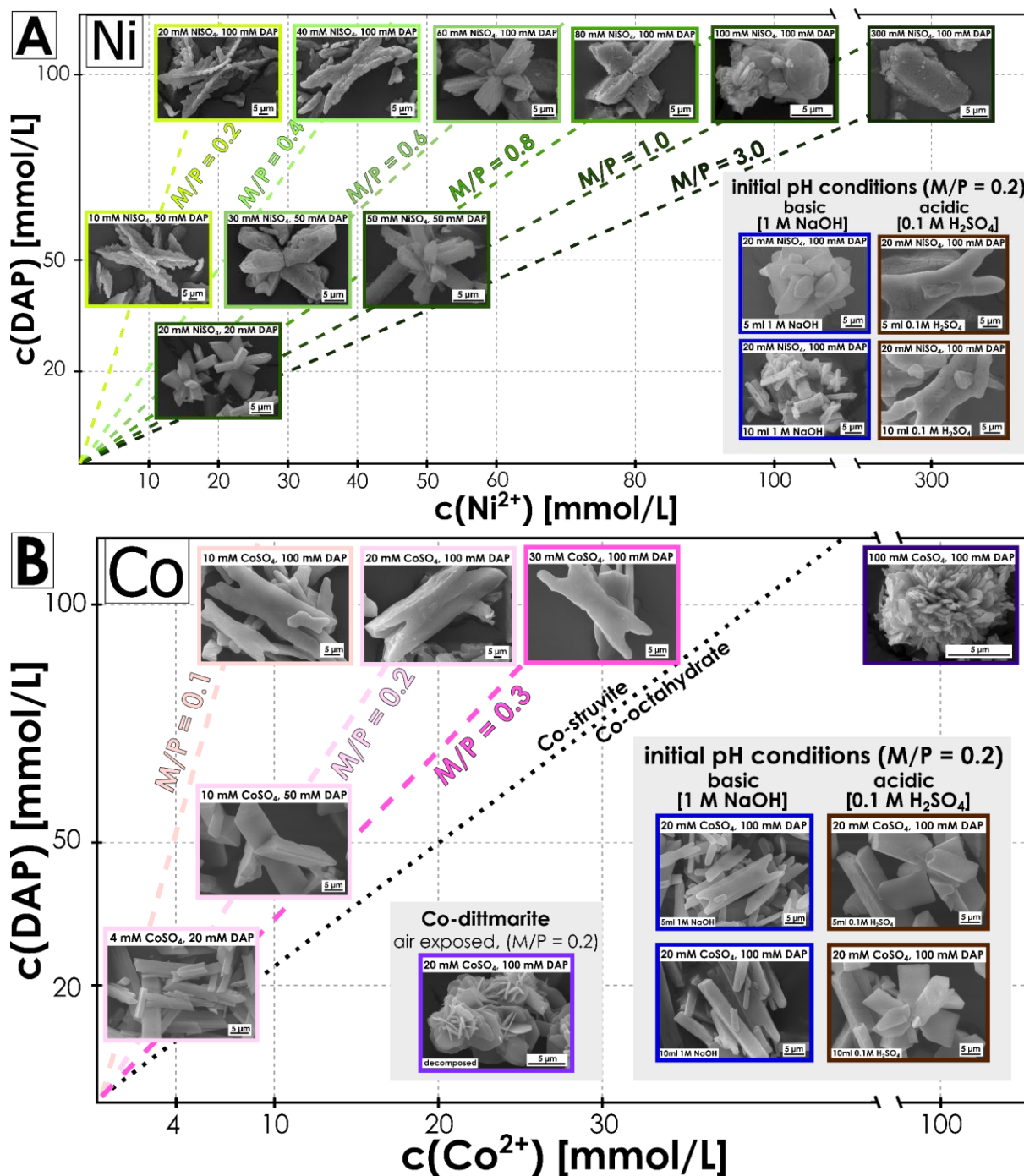


Figure 2: $c(M^{2+})$ vs. $c(DAP)$ plot with (A) green (for Ni) and (B) pink (for Co); color frames and dotted lines indicate the distinct M/P ratio of the sample; lower right left corner: pH samples with a M/P ratio = 0.2 (0.02 M $NiSO_4/CoSO_4$, 0.1 M DAP) with different initial amounts of 1 M $NaOH_{(aq)}$ (blue frames) or 0.1 M $H_2SO_{4(aq)}$ (brown frames); in air Co-struvite decomposed to Co-dittmarite with a M/P ratio = 0.2, and is displayed in (B).

Due to the limited stability of Co-struvite, only samples with the ratio below 0.4 could be analyzed. Above the ratio of 0.4 only Co-octahydrate is stable. At a constant ratio the crystallite size increased from $16 \pm 5 \mu m$ with 4 mM Co^{2+} and 20 mM DAP to $60 \pm 13 \mu m$ with 20 mM Co^{2+} and 100 mM DAP. The Co system followed a similar, but less-pronounced correlation to the one seen for the Ni. High DAP concentrations favored the formation of large euhedral crystals while higher Co^{2+} contents led to small anhedral crystals. Similarly to Ni-struvite, Co-struvite exhibited X-shaped crystal morphologies at high $c(DAP) \geq 50$ mM and low M/P ratios < 0.3 , but the crystallographic planes were anhedrally developed (Figure 2B, SI: Figure S11).

The “coffin-like” habit occurred at low M/P ratios < 0.3 and low $c(\text{DAP}) \leq 50$ mM. Co-octahydrate showed a rough two-dimensional flake- or sheet-shaped morphology of the crystals and formed big crystal agglomerates of several μm . Co-dittmarite demonstrated a similar habit of regularly arranged plates, also reported in other studies³⁴. By increasing the pH with NaOH the crystal habit changed from a X-shaped morphology to elongated rod or prism-like habit (grey insets in Figure 2, SI: Figure S12). Here, the 5 ml 1 M $\text{NaOH}_{(\text{aq})}$ sample indicates remarkably the transition between those two morphologies. 10 ml $\text{NaOH}_{(\text{aq})}$ decreased the crystallite size from 60 ± 13 μm to 23 ± 6 μm . Adding $\text{H}_2\text{SO}_{4(\text{aq})}$ favored the formation of tabular-shaped Co-struvites with slightly decreased size of 35 ± 8 μm . All trends in terms of crystal morphology and size for Ni and Co are summarized in the SI (SI: Figure S13). Mg-struvite is a relatively extensively investigated mineral phase^{27, 36, 39}, and therefore it was synthesized to serve as a reference for transition metal phosphates (see SI: Figure S14). At high concentrations of DAP and Mg^{2+} struvite formed an X-shaped crystal habit with a crystallite size of 120 ± 20 μm , while at low concentrations orthorhombic prisms were observed and the crystallite size decreased to 40 ± 6 μm . In the case when we adjusted conditions to be initially acidic (adding 10 ml of 0.1 M H_2SO_4 with a pH = 1.00) the struvite crystals were comparable in terms of shape and size to those observed in the pH unadjusted samples. However, the surface exhibited features of acidic leaching. Under basic conditions adding 10 ml of 1 M $\text{NaOH}_{(\text{aq})}$, the size of the crystallites got reduced to 5 ± 2 μm and the shape changed to more rounded orthorhombic prisms, but in contrast to acidic conditions the crystal surface were visually not affected.

These results demonstrate a controllable and tunable adjustment of the crystallite size, morphology, and composition of M-struvites through changes in the reaction conditions.

Stability of phases from the point of coordination environment

Crystalline M-struvites form in both transitional metal systems (Ni^{2+} , Co^{2+}), but they exhibit different stability. Namely, Co-struvite decomposes in air to Co-dittmarite while Ni-struvite remains stable. The observed instability of crystalline Co-struvite is quite surprising, and as we show below, is not caused by oxidation of Co^{2+} . Instead, these differences can be explained in the context of the local coordination environment of the MO_6 octahedron in the struvite structure. To evaluate how the stability of Ni and Co phosphates is related to their coordination environment in the crystal structure and how they differ between each other, EXAFS measurements were performed (Figure 3, SI: Figure S15). In general, XAS analysis reveal quantitatively changes in oxidation state, in the local coordination geometry/symmetry and bond distances among the different Co- and Ni-phases. Especially the intensity of the pre-peak (XANES) which originates from the $1s$ - $3d$ transitions expresses the degree of centrosymmetry and coordination environment in the vicinity of the considered ions (SI: Figure S15, Table S4). As only $3d$ - $4p$ hybridization enable parity allowed transitions the extent of those is strongly correlated with the coordination geometry. Near-ideal centrosymmetric coordinations show very low pre-peak intensities while more distorted geometries exhibit higher intensities. Quantitative real-space fittings on the radial distribution function reveal the bond distances

in the first coordination environment around the Co^{2+} and Ni^{2+} metal cation and can be linked to the crystallographic structure (Figure 3).

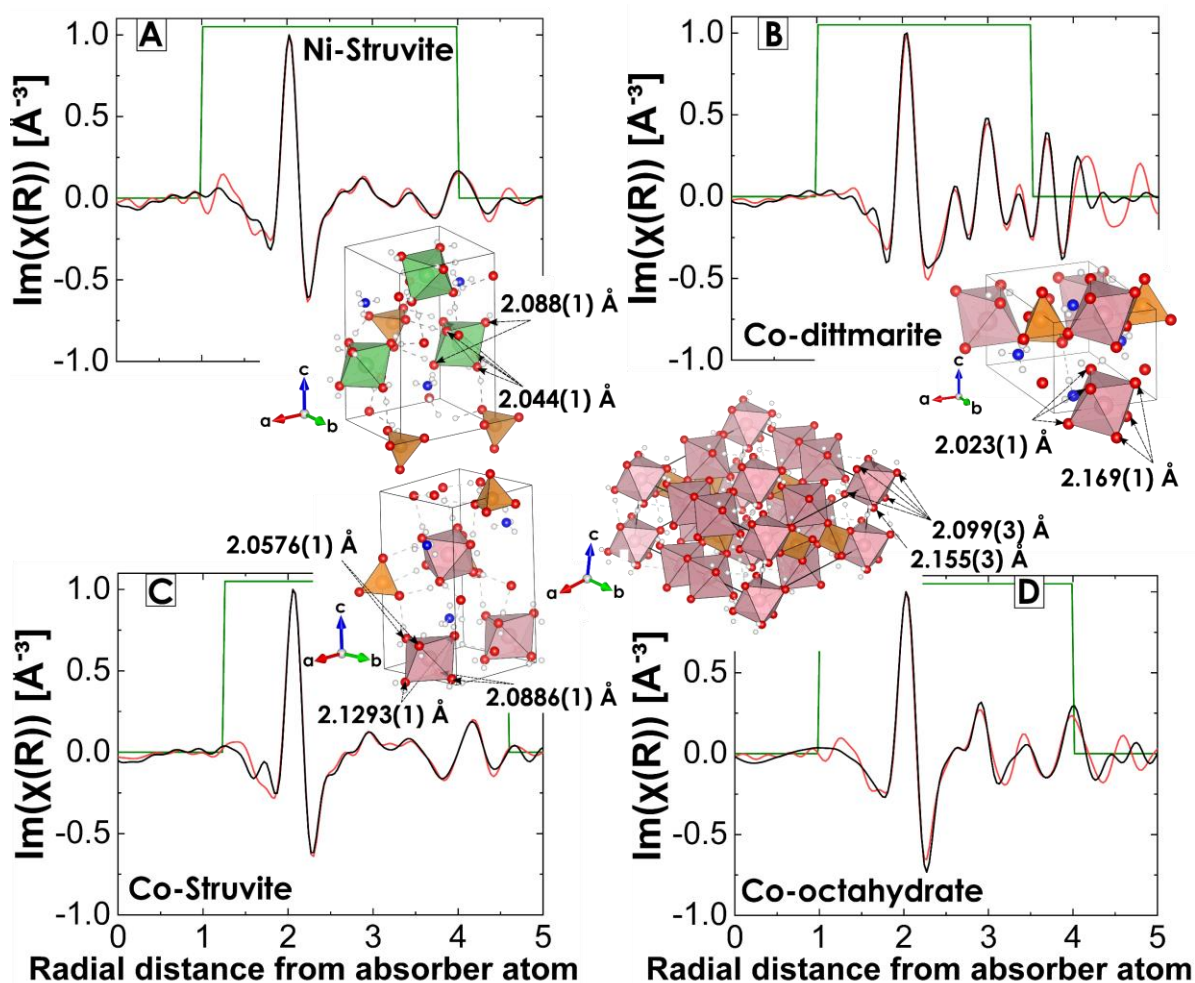


Figure 3: Ni- and Co K-edge EXAFS data shown in real space for (A) $\text{NH}_4\text{NiPO}_4 \cdot 6\text{H}_2\text{O}$ space group: $\text{Pmn}2_1$, $R = 0.005$; (B) for $\text{NH}_4\text{CoPO}_4 \cdot \text{H}_2\text{O}$ space group: $\text{Pmn}2_1$, $R = 0.008$; (C) $\text{NH}_4\text{CoPO}_4 \cdot 6\text{H}_2\text{O}$ space group: $\text{Pmn}2_1$, $R = 0.012$; and (D) $\text{Co}_3(\text{PO}_4)_2 \cdot 8\text{H}_2\text{O}$ space group: $\text{C}2/m$, $R = 0.005$; experimental data: red, fit results: black; fit window: green.

The XAS spectra (SI: Figure S15) clearly prove that Co and Ni are exclusively present as the bivalent species in all samples, as is evidenced by comparing with multiple M^{2+} standards (only $\text{MSO}_4 \cdot n\text{H}_2\text{O}$ is shown for clarity). No indication for incorporated oxidized Ni^{3+} or Co^{3+} was observed in the powders. Quantitative pre-peak integration results are summarized in Table S4. As it is indicated by a minimal pre-peak area ($A_{pp} = 0.0298(3)$) and a maximized intensity in the white line, Co-struvite as well as Ni-struvite ($A_{pp} = 0.0281(2)$) have a more centrosymmetric octahedral coordination environment compared to Co-dittmarite and Co-octahydrate ($A_{pp} = 0.0363(4)$ and $A_{pp} = 0.0355(4)$) (SI: Table S4). After FT of $\chi(k)$ into R-space radial distances from the absorber atom can be observed (SI: Figure S15C). At around $R \approx 1.9 \text{ \AA}$ all samples show a maximum which is related to the degeneracy of single scattering path of the Ni-O or Co-O bond length. In the case of single scattering, we have a direct measure of the coordination number (CN). The peak at $R \approx 2.7 \text{ \AA}$ in CPO and COD fits to the Co-P single scattering path, which is absent in the M-struvites. In CPO and COD the CoO_6 octahedrons are linked to four (CPO) or five (COD) O^{2-} of PO_4 tetrahedrons (short distance of Co-P) while in the

struvite structure they are isolated from the phosphate tetrahedron through coordination of six O^{2-} of water molecules (long distance of Ni-P and Co-P, SI: Figure S15). The slight color change among COS, COD and CPO of the chemical compounds of Co is related to the number and the distortion of the coordinating water molecules. The peak at $R \approx 3.8 \text{ \AA}$ consists of several single and multiple scattering paths such as Co-N, Co-H, Co-P, Co-O-O. All fitting parameters are shown in SI: Tables S5-S8. By calculating the mean bond distance and its sphere volume, a quantitative comparison of the coordination sphere is possible. The M-struvites (M-struvite Ni: 2.059(6) \AA Co: 2.091(1) \AA) demonstrate slightly lower mean bond distances than COD and CPO (CoD: 2.096(1) \AA , CPO: 2.11(2) \AA). The fitted bond distances are visualized with the calculated fits in Figure 3 for the different compounds (SI: Tables S5-S8).

Discussion

General phase selection, stability and transformations

In broad terms, whether an actual transition metal struvite might be a probable phase is determined by the M cation's charge and radius compared to Mg^{2+} . Considering the ionic radii of $Co^{2+[VI]}$ (0.75 \AA , high state) and $Ni^{2+[VI]}$ (0.69 \AA) compared to $Mg^{2+[VI]}$ (0.72 \AA), all ions have similar radii so they could be potentially substituted one for another in the struvite structure $Pmn2_1$ (SI: Figure S1A). However, in practice it is apparent that the crystallization pathways play a crucial role in the phase selection. In all the considered chemical systems crystalline M-struvites could be obtained, but the conditions and the nucleation pathways toward the final crystal varied among different cations. For all three metal cations, single-phase M-struvite was obtained within a specific reaction window (SI: Figure S1B-D), while specifically for Co at higher reactant concentration, phosphate octahydrate (CPO) is crystallizing instead of struvite. It was evident that for both Ni and, even more clearly for Co, the crystalline phases formed through transformation of amorphous phases accompanied by a color change. This transition of colors is highly significant because it points to specific meta-stable reaction products. For both Ni and Co systems amorphous phases play a role in the nucleation of struvite, as we discuss below. More significantly, in the case of Co, the early-stage speciation appears also to control the phase selection between struvite and CPO. During the formation of CPO at high reactant concentrations, since ammonium is the most abundant species in the aqueous solution, the dissociation equilibrium to ammonia with the release of protons dominates the pH. The remaining less abundant phosphate due to the M/P ratio in CPO of 3:2, and the coupled dissociation to $H_xPO_4^{3-x}$ species, with the removal of protons can only compensate to a limited extent. The jump of the pH after 1800 s (SI: Figure S5) could be influenced by the formation of $Co(NH_3)_xH_2O_{6-x}^{2+}$ aqua complexes indicated by a light pink color^{40, 41}. The 0.1 M concentrated Ni and Mg samples do not exhibit any late reduction of pH as most of the ammonium is bound in the struvites, and probably no amorphous metal phosphate phase is stable over a longer period (> several mins), although it is briefly yet clearly present for Ni.

Significance of amorphous phases for nucleation of struvite

Interestingly, Mg-struvite and Ni-struvite seem to have higher stability compared to Co-struvite, because no other phases precipitate in solution. From the pH trends (SI: Figure

S5), dry and cryo-TEM measurements combined with SAED patterns we found no indication or even hint for an amorphous phase in the Mg-system as the crystals grew immediately after mixing to μm size (Figure 1, SI: Figure S6). In contrast, short-lived amorphous nanophases occurred in the Ni-system which form in the early stages of precipitation within seconds. These regular amorphous agglomerates of spherical particles probably aggregate and transform at higher reaction times to a precursor “unit” of a crystal. The Co-system exhibits metastable long-lived (minutes to hours) amorphous phases on the way to the final crystalline Co-struvite, which is correlated with a color change from purple to light pink. Here, the Co^{2+} changes its configuration from tetrahedral to octahedral coordination which leads to a slightly different color absorption^{34, 35}. Similarly to the Ni-samples, cobalt formed round amorphous nanoparticles (Figure 1, SI: Figure S8). The condensation and densification to a proto-crystalline unit took place throughout a longer time period (mins to hours) than in the Ni-system. It may explain why only a weak correlation between concentration of $\text{Co}^{2+}/\text{DAP}$ and the resulting crystal habit is observed compared to Ni and Mg. Based on the results, it is clear that crystallization of transition metal struvites follows a non-classical nucleation pathway^{42, 43} which involves transitional amorphous precursor phases on the way to the final crystalline product (Figure 4). The amorphous colloidal nanoparticles form within seconds, aggregate and transform within minutes of reaction time. These aggregates transform to a proto-crystalline nucleus which facilitate the next crystallisation of new nuclei. In the final step depending on the reaction conditions these crystal nuclei develop into different morphologies and sizes of crystals.

Crystal morphology and phase

Following the formation of the crystals, a higher supersaturation leads to a higher nucleation rate which provides numerous crystal nuclei of smaller crystallite sizes. At low supersaturations only a few crystal nuclei grow significantly due to a lower nucleation rate. Based on observations, the Ni^{2+} and Co^{2+} concentration controls the struvite morphology in terms of the usual supersaturation and reaction kinetics. In addition, with increasing initial metal concentration, the presence of metal aqua complexes becomes more significant, where the complexes influence the crystallization through positive feedback for instance by “locking” available ammonium ions. Higher concentrations of DAP correlate with the apparent elongation and increasing crystallite size of the crystals at a constant M/P ratio. Similar effects were observed for the crystallization of Mg-struvites³⁹. As in DAP two moles of NH_4^+ are present, the effect of higher DAP concentrations on the crystals is mostly related to higher concentrations of ammonium.

In all systems an initial basic pH decreased the crystallite size significantly and stabilized a more rod/prism-like morphology of the crystals. An initial acidic pH remained the crystallite size practically unchanged in the Ni-system, but the crystal surface was clearly affected by the acid. In the Co-system the crystallite size decreased slightly to $\sim 10 \mu\text{m}$ and the morphology changed to more tabular shapes. The Co-samples treated with sulfuric acid exhibited a short presence of the transitional amorphous colloidal phases of 10-15 mins as well as they decomposed faster to Co-dittmarite within several hours compared to the pH unaffected

samples. Since only 0.1 M $\text{H}_2\text{SO}_{4(\text{aq})}$ was added initially in the amount sufficient not to dissolve the crystals completely, the absolute change in pH, $|\Delta\text{pH}|$, was lower and asymmetric than the one induced by adding higher concentrated 1 M $\text{NaOH}_{(\text{aq})}$ to the system. As an increase in the pH shifts the equilibrium to the side of the products in eq.[1], a high number of crystal nuclei are formed and grow simultaneously. Consequently, as many crystals of a low size have a higher surface area compared to few crystals of a larger size, these nuclei would grow only to a limited extent. Therefore, these crystals are much smaller than in the pH unadjusted runs where only few crystals grew large. Low-concentration sulfuric acid already reduces the lifespan of the transitional colloidal nanophases and the final crystalline Co-struvite significantly. From the point of view of saturation index (SI) and ion activity product (IAP), an initial basic pH increases the $\text{SI}_{\text{M-struvite}}$ as the activity of $[\text{PO}_4^{3-}_{(\text{aq})}]$ increases. However, this shift of the equilibrium to the product side is limited to a certain pH, because at a high pH (for Mg-struvite $\text{pH} = 11$) the presence of $\text{NH}_3^0_{(\text{aq})}$ and $\text{M}(\text{OH})^-_{(\text{aq})}$ species reduces the activities of $\text{NH}_4^+_{(\text{aq})}$ and M^{2+} and therefore compensates for the increase of activity of $\text{PO}_4^{3-}_{(\text{aq})}$ ³⁹.

Phase stability from a point of view of a metal coordination environment

Co-struvite exhibits low stability compared to Ni-struvite as it decomposes in air spontaneously to Co-dittmarite or is replaced at higher concentrations of $c(\text{Co}^{2+}) > 0.4$ by CPO as the most stable phase. This is quite surprising, in particular in the case of fully developed and supposedly thermodynamically stable crystals. Hints on these stability properties are hidden in the metal coordination environment. The CoO_6 octahedron in the struvite structure shows a higher degree of distortion compared to NiO_6 in Ni-struvite, but a lower one compared to the other Co-phases (see pre-peak area fits in **Error! Reference source not found.**). The volume and the distortion of the CoO_6 octahedron could expand simply the stability of the M-struvite structure and therefore, it tends to decompose to Co-dittmarite. Here, the Co-dittmarite structure allows for a more distorted coordination environment of the central metal cation since it is coordinated by five corner-linking O^{2-} anions of the phosphate tetrahedrons and one O^{2-} anion from the remaining crystal water (SI: Figure S15 and 16). This assumption takes into account the high stability of Co(II) phosphate octahydrate at high M/P ratios > 0.4 (Figure 2B, SI: Figure S1), where Co^{2+} is also bound in a similar distorted octahedral coordination as in Co-dittmarite (SI: Figure S16, Table S4). As H_2O behaves as a weak-field ligand for most of the bivalent transition metal ions, the high spin configuration is realized in their complexes. Looking at the Irving-Williams thermodynamic series of high spin first row transition metals in the bivalent oxidation state the stability of metal complexes decreases in the order $\text{Mn}^{2+} < \text{Fe}^{2+} < \text{Co}^{2+} < \text{Ni}^{2+} < \text{Cu}^{2+} > \text{Zn}^{2+}$ regardless of the type of coordinated ligands^{44, 45}. Co^{2+} as a d^7 ion shows a strong Jahn-Teller effect in octahedral coordination with weak ligands like H_2O (high-state) compared to Ni^{2+} with a d^8 orbitals as more unpaired electrons occur in this electron configuration. In agreement with our results, other studies demonstrated a distorted non-centrosymmetric octahedral coordination of Co^{2+} as d^7 ion in Co-doped Ni-struvite while Ni^{2+} as a d^8 ion exhibits a near ideal cubic octahedral coordination based on electron spin resonance spectroscopy⁴⁶. Therefore, we suggest that the different

stabilities of Ni- and Co-struvite are mainly influenced by the electronic d-configuration and their ionic radii for the struvite structure $Pm\bar{n}2_1$.

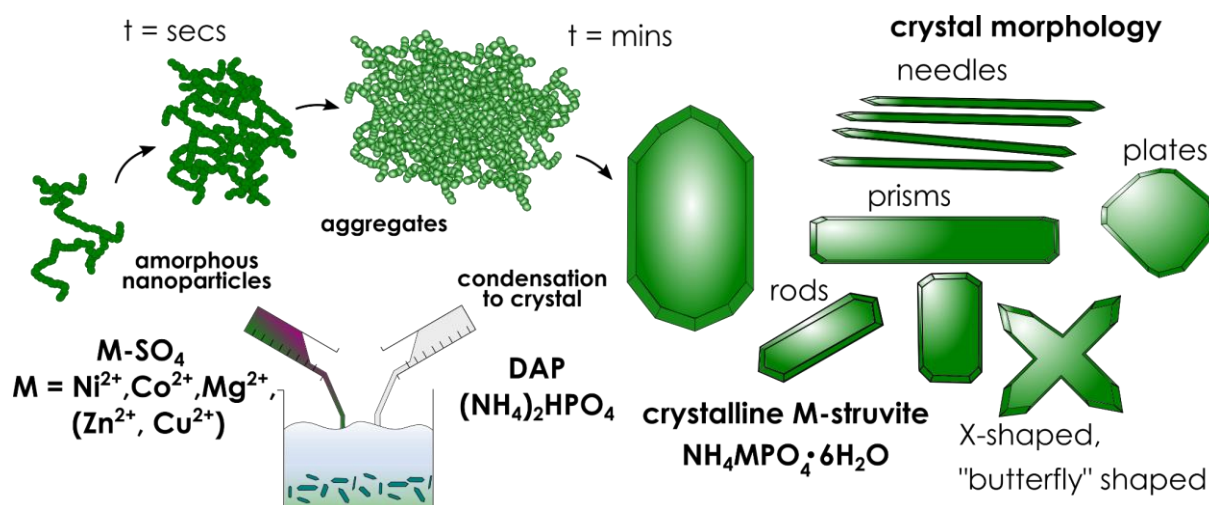


Figure 4: Visualization of the formation of different transition metal struvite crystals through a non-classical crystallization route including amorphous nanoparticles. Stages according to the labels.

Conclusion

Our investigation of transition metal struvites as potential systems for multicomponent precipitation led to several crucial insights. Ni-struvite is stable in multiple concentrations of the reactants and at different metal/phosphate (M/P) ratios. Co-struvite precipitates at a M/P ratio of 0.4, whereas above this value only Co(II)-phosphate octahydrate is stable. Ni- and Co struvites form amorphous precursor phases on the way to the final crystalline product while no nanophase was observed for Mg. Control of different morphologies and sizes of transition metal struvite can be achieved depending on the crystallization conditions. Transition metal phosphates appear to form through non-classical nucleation pathways, which involve multiple amorphous nanophases during precipitation. Due to the low solubility product and their controlled precipitation through adjusting the reaction conditions transition metal struvite is a promising recovery material for extracting NH_4^+ , PO_4^{3-} and transition metals at simultaneously, out of agricultural and mine wastewaters. Furthermore, the possibility to specifically set/tune the morphology and properties opens the prospect of up-cycling materials directly as raw materials for applications (e.g. electrocatalysis).

Acknowledgements

We acknowledge Uwe Reinholz, Martin Radtke and Kirill Yusenko for their support at the BAMline beamline of BESSY II. We acknowledge BAM and Helmholtz-Zentrum Berlin (HZB) for providing us with the beamtime at BESSY II. We thank Carsten Prinz for TEM measurements.

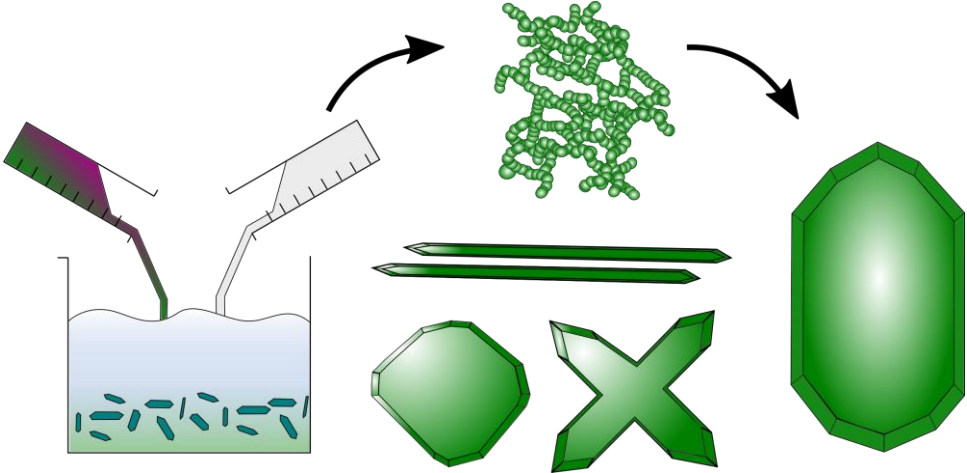
References

1. Cordell, D.; Drangert, J.-O.; White, S., The story of phosphorus: Global food security and food for thought. *Global Environmental Change* **2009**, *19*, (2), 292-305.
2. Filippelli, G. M., The Global Phosphorus Cycle. *Reviews in Mineralogy and Geochemistry* **2002**, *48*, (1), 391-425.
3. Gislev, M.; Grohol, M.; Mathieux, F.; Ardenne, F. *Report on Critical Raw Materials in the Circular Economy*; European Commission: 2018.
4. Neset, T. S.; Cordell, D., Global phosphorus scarcity: identifying synergies for a sustainable future. *J Sci Food Agric* **2012**, *92*, (1), 2-6.
5. Hallas, J.; Mackowiak, C.; Wilkie, A.; Harris, W., Struvite Phosphorus Recovery from Aerobically Digested Municipal Wastewater. *Sustainability* **2019**, *11*, (2).
6. Prot, T.; Korving, L.; Dugulan, A. I.; Goubitz, K.; van Loosdrecht, M. C. M., Vivianite scaling in wastewater treatment plants: Occurrence, formation mechanisms and mitigation solutions. *Water Res* **2021**, *197*, 117045.
7. Le Corre, K. S.; Valsami-Jones, E.; Hobbs, P.; Parsons, S. A., Phosphorus Recovery from Wastewater by Struvite Crystallization: A Review. *Critical Reviews in Environmental Science and Technology* **2009**, *39*, (6), 433-477.
8. El Diwani, G.; El Rafie, S.; El Ibiari, N. N.; El-Aila, H. I., Recovery of ammonia nitrogen from industrial wastewater treatment as struvite slow releasing fertilizer. *Desalination* **2007**, *214*, (1-3), 200-214.
9. Uysal, A.; Yilmazel, Y. D.; Demirer, G. N., The determination of fertilizer quality of the formed struvite from effluent of a sewage sludge anaerobic digester. *J Hazard Mater* **2010**, *181*, (1-3), 248-54.
10. Hao, X.; Wang, C.; van Loosdrecht, M. C.; Hu, Y., Looking beyond struvite for P-recovery. *Environ Sci Technol* **2013**, *47*, (10), 6-4965.
11. Sena, M.; Seib, M.; Noguera, D. R.; Hicks, A., Environmental impacts of phosphorus recovery through struvite precipitation in wastewater treatment. *Journal of Cleaner Production* **2021**, *280*.
12. Zhao, H.; Yuan, Z. Y., Insights into Transition Metal Phosphate Materials for Efficient Electrocatalysis. *ChemCatChem* **2020**, *12*, (15), 3797-3810.
13. Lin, R.; Ding, Y., A Review on the Synthesis and Applications of Mesostructured Transition Metal Phosphates. *Materials (Basel)* **2013**, *6*, (1), 217-243.
14. Xu, X.; Du, P.; Guo, T.; Zhao, B.; Wang, H.; Huang, M., In situ Grown Ni phosphate@Ni₁₂P₅ Nanorod Arrays as a Unique Core-Shell Architecture: Competitive Bifunctional Electrocatalysts for Urea Electrolysis at Large Current Densities. *ACS Sustainable Chemistry & Engineering* **2020**, *8*, (19), 7463-7471.
15. Meguerdichian, A. G.; Jafari, T.; Shakil, M. R.; Miao, R.; Achola, L. A.; Macharia, J.; Shirazi-Amin, A.; Suib, S. L., Synthesis and Electrocatalytic Activity of Ammonium Nickel Phosphate, [NH₄]NiPO₄·6H₂O, and beta-Nickel Pyrophosphate, beta-Ni₂P₂O₇: Catalysts for Electrocatalytic Decomposition of Urea. *Inorg Chem* **2018**, *57*, (4), 1815-1823.
16. Huang, H.; Xu, C.; Zhang, W., Removal of nutrients from piggery wastewater using struvite precipitation and pyrogenation technology. *Bioresour Technol* **2011**, *102*, (3), 8-2523.
17. Münch, E. V.; Barr, K., Controlled struvite crystallisation for removing phosphorus from anaerobic digester sidestreams. *Water Research* **2001**, *35*, (1), 151-159.
18. Zhangchen, R.; Liu, W. G., Q.; ; Ji, H.; Li, Y.; Zhang, J.; Song, J.; Zhong, Y.; Zhou, L., Struvite as seed materials for treatment of heavy metals in wastewater. *IOP Conference Series: Earth and Environmental Science (EES)* **2021**, *770*, 1-5.

19. Rouff, A. A., Sorption of chromium with struvite during phosphorus recovery. *Environ Sci Technol* **2012**, *46*, (22), 12493-501.
20. Rouff, A. A.; Juarez, K. M., Zinc interaction with struvite during and after mineral formation. *Environ Sci Technol* **2014**, *48*, (11), 6342-9.
21. Lu, X.; Huang, Z.; Liang, Z.; Li, Z.; Yang, J.; Wang, Y.; Wang, F., Co-precipitation of Cu and Zn in precipitation of struvite. *Sci Total Environ* **2021**, *764*, 144269.
22. Lin, J.; Chen, N.; Pan, Y., Arsenic incorporation in synthetic struvite (NH₄MgPO₄·6H₂O): a synchrotron XAS and single-crystal EPR study. *Environ Sci Technol* **2013**, *47*, (22), 35-12728.
23. Ravikumar, R.; Chandrasekhar, A.; Rama Krishnar, C.; Reddy, Y., X-ray powder diffraction, thermal analysis and IR studies of zinc ammonium phosphate hexahydrate. *Optoelectronics and Advanced Materials -Rapid Communciations* **2010**, *4*, 215-219.
24. Abbona, F.; Angela-Frachini, M.; Croni Bono, C.; Lundager Madsen, H., Effect of ammonia excess on the crystal habit of NiNH₄PO₄·6H₂O (Ni-struvite). *Journal of Crystal Growth* **1994**, *143*, 256-260.
25. Haferburg, G.; Kloess, G.; Schmitz, W.; Kothe, E., "Ni-struvite" - a new biomineral formed by a nickel resistant *Streptomyces acidiscabies*. *Chemosphere* **2008**, *72*, (3), 517-23.
26. Hövelmann, J.; Stawski, T. M.; Freeman, H. M.; Besselink, R.; Mayanna, S.; Perez, J. P. H.; Hondow, N. S.; Benning, L. G., Struvite Crystallisation and the Effect of Co²⁺ Ions. *Minerals* **2019**, *9*, (9).
27. Hovelmann, J.; Stawski, T. M.; Besselink, R.; Freeman, H. M.; Dietmann, K. M.; Mayanna, S.; Pauw, B. R.; Benning, L. G., A template-free and low temperature method for the synthesis of mesoporous magnesium phosphate with uniform pore structure and high surface area. *Nanoscale* **2019**, *11*, (14), 6939-6951.
28. Zhao, Y.; Chen, Z.; Xiong, D. B.; Qiao, Y.; Tang, Y.; Gao, F., Hybridized Phosphate with Ultrathin Nanoslices and Single Crystal Microplatelets for High Performance Supercapacitors. *Sci Rep* **2016**, *6*, 17613.
29. Parkhurst, D. L.; Appelo, C. A. J., *Description of input and examples for PHREEQC version 3: a computer program for speciation, batch-reaction, one-dimensional transport, and inverse geochemical calculations*. U.S. Geological Survey: Reston, VA, 2013.
30. Madsen, H. E. L., Solubility Product of Ni-Struvite, NH₄NiPO₄·6H₂O, at 25°C. *Advances in Chemical Engineering and Science* **2017**, *07*, (02), 206-214.
31. Görner, W.; Hentschel, M. P.; Müller, B. R.; Riesemeier, H.; Krumrey, M.; Ulm, G.; Dietsch, W.; Klein, U.; Frahm, R., BAMline: the first hard X-ray beamline at BESSY II. *Nuclear Instruments and Methods in Physics Research A* **2001**, *467-468*, 703-706.
32. Ravel, B.; Newville, M., ATHENA, ARTEMIS, HEPHAESTUS: data analysis for X-ray absorption spectroscopy using IFFFIT. *J Synchrotron Radiat* **2005**, *12*, (4), 537-41.
33. Momma, K.; Izumi, F., VESTA: a three-dimensional visualization system for electronic and structural analysis. *Journal of Applied Crystallography* **2008**, *41*, (3), 653-658.
34. Bach, S.; Visnow, E.; Panthöfer, M.; Gorelik, T.; Buzanich, A. G.; Gurlo, A.; Kolb, U.; Emmerling, F.; Lind, C.; Tremel, W., Hydrate Networks under Mechanical Stress - A Case Study for Co₃(PO₄)₂·8H₂O. *European Journal of Inorganic Chemistry* **2016**, *2016*, (13-14), 2072-2081.
35. Bach, S.; Panthöfer, M.; Bienert, R.; Buzanich, A. G.; Emmerling, F.; Tremel, W., Role of Water During Crystallization of Amorphous Cobalt Phosphate Nanoparticles. *Crystal Growth & Design* **2016**, *16*, (8), 4232-4239.

36. Crutchik, D.; Garrido, J. M., Struvite crystallization versus amorphous magnesium and calcium phosphate precipitation during the treatment of a saline industrial wastewater. *Water Sci Technol* **2011**, *64*, (12), 7-2460.
37. Zhang, Q.; Jiang, Y.; Gou, B.-D.; Huang, J.; Gao, Y.-X.; Zhao, J.-T.; Zheng, L.; Zhao, Y.-D.; Zhang, T.-L.; Wang, K., In Situ Detection of Calcium Phosphate Clusters in Solution and Wet Amorphous Phase by Synchrotron X-ray Absorption Near-Edge Spectroscopy at Calcium K-Edge. *Crystal Growth & Design* **2015**, *15*, (5), 2204-2210.
38. Mahamid, J.; Sharir, A.; Weiner, S., Amorphous calcium phosphate is a major component of the forming fin bones of zebrafish: Indications for an amorphous precursor phase. *PNAS* **2008**, *105*, 12748-12753.
39. Shaddel, S.; Ucar, S.; Andreassen, J. P.; Osterhus, S. W., Enhancing efficiency and economics of phosphorus recovery process by customizing the product based on sidestream characteristics - an alternative phosphorus recovery strategy. *Water Sci Technol* **2019**, *79*, (9), 1777-1789.
40. Blyholder, G.; Ford, N., Far-Infrared Spectra of some Mono- and Polynuclear Aqua-Substituted cobalt-Ammine Complexes. *The Journal of Physical Chemistry* **1964**, *68*, (6), 1496-1500.
41. Schmiedekamp, A. M.; Ryan, M. D.; Deeth, R. J., Six-Coordinate Co²⁺ with H₂O and NH₃ Ligands: Which Spin State Is More Stable? *Inorganic Chemistry* **2002**, *41*, 5733-5743.
42. De Yoreo, J., Crystal nucleation: more than one pathway. *Nat Mater* **2013**, *12*, (4), 5-284.
43. Andreassen, J.-P.; Lewis, A. E., Classical and Nonclassical Theories of Crystal Growth. In *New Perspectives on Mineral Nucleation and Growth*, 2017; pp 137-154.
44. Irving, H.; Williams, R., Order of stability of metal complexes. *Nature* **1948**, *162*.
45. Irving, H.; Williams, R., The stability of transition-metal complexes. *J. Chem. Soc.* **1953**, 3192-3210.
46. Foglio, M. B., G., Study of Co²⁺ in Different Crystal Field Environments. *Brazilian Journal of Physics* **2005**, *36*, 40-54.

Graphical abstract



Supporting Information for:

Ni- and Co-struvites: Revealing crystallization mechanisms and crystal engineering for phosphorous and transition metal recovery

Stephanos Karafiludis^{1*}, Ana Guilherme Buzanich¹, Zdravko Kochovski², Ines Feldmann¹, Franziska Emmerling^{1,3}, and Tomasz M. Stawski^{1**}

¹Federal Institute for Materials Research and Testing, Richard-Willstätter-Straße 11, 12489 Berlin, Germany;

²Department for Electrochemical Energy Storage, Helmholtz-Zentrum Berlin for Materials and Energy, Hahn-Meitner Platz 1, 14109 Berlin, Germany;

³Department of Chemistry, Humboldt-Universität zu Berlin, Brook-Taylor-Straße 2, 12489 Berlin

Corresponding authors: **tomasz.stawski@bam.de; *stephanos.karafiludis@bam.de

List of Tables

Table S1: Detailed reaction conditions for the precipitated samples	3
Table S2: PHREEQC calculations of pH changes in solution.	4
Table S3: Concentrations of Co, Ni, ammonia NH ₄ ⁺ and phosphate PO ₄ ³⁻ in different wastewaters	5
Table S4: Pre-peak integration results by fitting Gaussian functions with all fitting parameters	5
Table S5: ARTEMIS fit parameter for Ni-struvite R-factor= 0.005.....	6
Table S6: ARTEMIS fit parameter for Co-struvite R-factor= 0.012.....	7
Table S7: ARTEMIS fit parameter for Co-dittmarite (COD), R-factor= 0.008.	8
Table S8: ARTEMIS fit parameter for Co-phosphate octahydrate (CPO), R-factor= 0.005.	9

List of Figures

Figure S1: Phase stability diagrams of Mg, Ni and Co samples	10
Figure S2: XRD patterns of M-phosphates synthesized with different reactant concentrations	11
Figure S3: Additional XRD patterns of Co phosphates.	12
Figure S4: XRD patterns of pH adjusted samples with NaOH _(aq) and H ₂ SO _{4(aq)}	13
Figure S5: pH measurements of high (0.1 M) and low (0.02 M) metal concentrations	14
Figure S6: detailed dry TEM image of Mg-sample with EDS point measurements after 5 s mixing.....	14
Figure S7: dry STEM and cryo TEM images of Ni sample with SAED pattern, EDS mappings and point measurements after 5 s mixing.....	15
Figure S8: dry STEM and cryo TEM images of Co sample with SAED pattern, EDS mappings and point measurements after 5 s mixing.....	16
Figure S9: SE images of Ni-struvite samples synthesized in different reactant concentrations	17
Figure S10: SE images of Ni-struvite samples synthesized in different initial pH.	18
Figure S11: SE images of Co phosphate samples synthesized in different reactant concentrations....	19
Figure S12: SE images of Co-struvite samples synthesized in different initial pH.....	20
Figure S13: Crystallization trends in the c(M ²⁺) vs. c(DAP) plots of Ni and Co	21
Figure S14: SE images of mg-struvite samples synthesized in different reactant concentrations	22
Figure S15: XAS spectra of Co and Ni samples with detailed view of the pre-peak region and Fourier-transformed spectra plotted in R-space.....	23
Figure S16: Crystallographic differences between the Co phosphate phases	24

Contents

Supplementary Note 1	25
Supplementary Note 2	26
References SI.....	27

Table S1: Detailed reaction conditions for the precipitated samples.

c(NiSO₄)	c(DAP)	M/P ratio	c(CoSO₄)	c(DAP)	M/P ratio	c(MgCl₂)	c(DAP)	M/P ratio
[M]	[M]		[M]	[M]		[M]	[M]	
0.004	0.02	0.2	0.004	0.02	0.2	0.004	0.02	0.2
0.01	0.05	0.2	0.008	0.02	0.4	0.01	0.05	0.2
0.012	0.02	0.6	0.01	0.05	0.2	0.012	0.02	0.6
0.02	0.02	1	0.012	0.02	0.6	0.02	0.02	1
0.02	0.1	0.2	0.02	0.02	1	0.02	0.1	0.2
0.03	0.05	0.6	0.02	0.1	0.2	0.03	0.05	0.6
0.04	0.1	0.4	0.03	0.05	0.6	0.04	0.1	0.4
0.05	0.05	1	0.04	0.1	0.4	0.05	0.05	1
0.06	0.1	0.6	0.042	0.1	0.42	0.06	0.1	0.6
0.08	0.1	0.8	0.046	0.1	0.46	0.08	0.1	0.8
0.1	0.1	1	0.05	0.05	1	0.1	0.1	1
0.15	0.1	1.5	0.05	0.1	0.5	0.15	0.1	1.5
0.3	0.1	3	0.054	0.1	0.54	0.3	0.1	3
			0.058	0.1	0.58			
			0.06	0.1	0.6			
			0.08	0.1	0.8			
			0.1	0.1	1			
			0.15	0.1	1.5			
			0.3	0.1	3			

Table S2: PHREEQC calculations of pH changes in solution with 100 ml 0.1 M DAP and 100 ml of 0.02 M M^{2+} (M = Mg, Co, Ni) with different amounts of 1 M $NaOH_{(aq)}$ (pH = 13.97) and 0.1 M $H_2SO_{4(aq)}$ (pH = 1.00).

Experimental conditions		M/P ratio = 0.2		c(MSO ₄) [mM] = 20		c(DAP) [mM] = 100	
Sample with normal pH	amount of 1M $NaOH_{(aq)}$ [ml]	calculated pH _{eq}	ΔpH	amount of 0.1M $H_2SO_{4(aq)}$ [ml]	calculated pH _{eq}	ΔpH	
Ni-struvite pH _{eq} = 6.87	1	7.03	0.16	1	6.82	-0.05	
	2	7.21	0.33	2	6.78	-0.10	
	3	7.40	0.53	3	6.73	-0.15	
	4	7.66	0.78	4	6.68	-0.20	
	5	8.04	1.17	5	6.63	-0.25	
	6	8.47	1.60	6	6.57	-0.30	
	7	8.78	1.90	7	6.52	-0.35	
	8	8.99	2.12	8	6.46	-0.42	
	9	9.17	2.30	9	6.41	-0.47	
	10	9.32	2.45	10	6.35	-0.53	
Co-struvite pH _{eq} = 7.02	1	7.18	0.16	1	6.98	-0.04	
	2	7.37	0.35	2	6.94	-0.08	
	3	7.60	0.58	3	6.90	-0.12	
	4	7.89	0.87	4	6.86	-0.16	
	5	8.19	1.17	5	6.83	-0.19	
	6	8.38	1.36	6	6.79	-0.23	
	7	8.51	1.49	7	6.76	-0.26	
	8	8.59	1.57	8	6.72	-0.30	
	9	8.66	1.64	9	6.67	-0.35	
	10	8.75	1.73	10	6.61	-0.41	
Mg-struvite pH _{eq} = 7.33	5	8.86	1.84	5	6.99	-0.03	
	10	9.45	2.43	10	6.71	-0.62	

Table S3: Concentrations of Co, Ni, ammonia NH_4^+ and phosphate PO_4^{3-} /total phosphorus (TP) in different wastewaters in mg/L, otherwise unit displayed; agricultural wastewaters contain high amounts of ammonia and phosphorus while mine wastewaters exhibit high concentrations of heavy metals.

country	region	waste water	species	concentration	reference
DRC	Katanga province	mine wastewater	Co	3.164	Atibu et al.2013 ¹
Italy	Rio Piscinas	ground water (contaminated)	Co	2.9-1.5	Concas et al. 2006 ²
			Ni	4.6-3.0	
Turkey	Amik plain	agricultural wastewater	NH_4^+	13	Agca et al. 2014 ³
			TP	87	
			Co	13 [$\mu\text{g/L}$]	
			Ni	50 [$\mu\text{g/L}$]	
USA	Duluth gabbro, Minnesota	mine wastewater	Co	9.8	Hammack et al. 1991 ⁴
			Ni	198	
Jordan	Eshidiya mine	mine wastewater	NH_4^+	95-30[$\mu\text{g/L}$]	Al-Hwaiti et al. 2016 ⁵
			PO_4^{3-}	8.9-0.1	
		ground water	NH_4^+	3.8-3.5	Al-Hwaiti et al. 2016 ⁵
			PO_4^{3-}	50-10 [$\mu\text{g/L}$]	
Zambia	Kabwe	mine wastewater	Co	34,400	Sracek et al. .2010 ⁶
China	Sichuan	agricultural wastewater	NH_4^+	1257.14	Feng et al. 2020 ⁷
			PO_4^{3-}	25.01	
Brazil		agricultural wastewater	NH_4^+	77	Leite et al. 2009 ⁸
			TP	12	
USA	Cobalt, Ontario	surface water	Co	2028-0.5 [$\mu\text{g/L}$]	Percival et al. 1996 ⁹
			Ni	660-2.6 [$\mu\text{g/L}$]	
Serbia	Bor	mine wastewater	Ni	6128	Stopic et al. 2007 ¹⁰
			Co	1.2	

Table S4: Pre-peak integration results by fitting Gaussian functions with all fitting parameters; Pre-peak fits visible in Figure S15.

Sample	Prepeak area integration results			fit function: Gaussian		
	chemical formula	R ² value	Pre-peak Area A _{pp} (err)	FWHM	Center	Max. Height
Co-octahydrate	$\text{Co}_3(\text{PO}_4)_2 \cdot 8\text{H}_2\text{O}$	0.995	0.0363(4)	2.296	7711.2	0.0149
Co-dittmarite	$\text{NH}_4\text{CoPO}_4 \cdot \text{H}_2\text{O}$	0.991	0.0355(4)	2.101	7711.5	0.0159
Co-struvite	$\text{NH}_4\text{CoPO}_4 \cdot 6\text{H}_2\text{O}$	0.993	0.0298(3)	2.314	7711.1	0.0121
Ni-struvite	$\text{NH}_4\text{NiPO}_4 \cdot 6\text{H}_2\text{O}$	0.992	0.0281(2)	1.969	8333.3	0.0134

Table S5: ARTEMIS fit parameter for Ni-struvite R-factor= 0.005.

sample	scattering path	degeneracy	σ^2	R_{diff} [Å]	R_{diff}^2 [Å ²]	R_{model} [Å]	R_{fit} [Å]
Ni-struvite	Ni1-O1	4	0.009	-0.001	1.00E-06	2.046	2.044
NH₄NiPO₄•6H₂O	Ni1-O2	2	0.009	-0.001	1.00E-06	2.089	2.088
mean R_{fit} (err) [Å]	Ni1-O3 H1	4	-0.001	-0.207	4.29E-02	2.560	2.353
2.059(6)	Ni1-H2	5	0.012	-0.217	4.70E-02	2.586	2.369
V_{sphere} (err) [Å ³]	Ni1-H3	2	0.012	-0.217	4.70E-02	2.627	2.410
36.6 (2)	Ni1-H4	2	0.012	-0.217	4.70E-02	2.668	2.451
R-factor	Ni1-O1-O1	6	-0.001	-0.207	4.29E-02	3.465	3.258
0.005	Ni1-O3-O2	16	-0.001	-0.207	4.29E-02	3.530	3.322
S_o^2 Amplitude reduction factor (err)	Ni1-N1	1	0.005	-0.186	3.47E-02	4.022	3.836
1.3(1)	Ni1-N2	2	0.005	-0.186	3.47E-02	4.111	3.925
ΔE	Ni1-O4	4	0.006	0.242	5.85E-02	4.084	4.326
3.1(6)	Ni1-O5	2	0.006	0.242	5.85E-02	4.162	4.404
	Ni1-O6	2	0.006	0.242	5.85E-02	4.200	4.442
	Ni1-O7	3	0.006	0.242	5.85E-02	4.272	4.514
	Ni1-O8	2	0.006	0.242	5.85E-02	4.329	4.571

Table S6: ARTEMIS fit parameter for Co-struvite R-factor= 0.012.

sample	scattering path	degeneracy	σ^2	$R_{\text{diff}} [\text{\AA}]$	$R_{\text{diff}}^2 [\text{\AA}^2]$	$R_{\text{model}} [\text{\AA}]$	$R_{\text{fit}} [\text{\AA}]$
Co-struvite	Co1-O1	2	0.005	0.0001	1.69E-08	2.058	2.058
NH₄CoPO₄•6H₂O	Co1-O2	2	0.005	0.0001	1.69E-08	2.089	2.089
mean R_{fit} (err) [\AA]	Co1-O3	2	0.005	0.0001	1.69E-08	2.129	2.129
2.091(1)	Co1-H1	2	0.003	0.3078	9.48E-02	2.211	2.519
V_{sphere} (err) [\AA^3]	Co1-H2	2	0.003	0.3078	9.48E-02	2.451	2.759
38.35(2)	Co1-H3	4	0.003	0.3078	9.48E-02	2.549	2.857
R-factor	Co1-H4	2	0.003	0.3078	9.48E-02	2.616	2.924
0.012	Co1-O1-H3-O1	4	0.003	0.3774	1.42E-01	2.752	3.129
S_{O}^2 Amplitude reduction factor (err)	Co1-O5-O6-O5	2	0.003	0.3774	1.42E-01	2.840	3.217
0.85(5)	Co1-O3-H5-O3	1	0.003	0.3774	1.42E-01	2.843	3.220
ΔE	Co1-O1-O2	6	-0.003	0.2301	5.29E-02	3.507	3.737
4.5(6)	Co1-O1-O3	12	-0.003	0.2301	5.29E-02	3.575	3.805
	Co1-O2-O3	4	-0.003	0.2301	5.29E-02	3.622	3.852
	Co1-N1	1	0.001	-0.0171	2.94E-04	4.027	4.009
	Co1-N2	2	0.001	-0.0171	2.94E-04	4.133	4.115
	Co1-O4	4	0.003	0.3774	1.42E-01	4.105	4.482
	Co1-O6	4	0.003	0.3774	1.42E-01	4.199	4.576
	Co1-O7	3	0.003	0.3774	1.42E-01	4.288	4.665
	Co1-O8	2	0.003	0.3774	1.42E-01	4.362	4.739
	Co1-P1	2	0.003	0.3774	1.42E-01	4.393	4.770

Table S7: ARTEMIS fit parameter for Co-dittmarite (COD), R-factor= 0.008.

sample	scattering path	degeneracy	σ^2	R_{diff} [Å]	R_{diff}^2 [Å ²]	R_{model} [Å]	R_{fit} [Å]
Co-dittmarite	Co1-O1	3	0.001	0.0001	1.69E-08	2.055	2.023
NH ₄ CoPO ₄ •H ₂ O	Co1-O2	3	0.001	0.0001	1.69E-08	2.201	2.169
mean R_{fit} (err) [Å]	Co1-H1	2	-0.008	0.0001	1.69E-08	2.492	2.222
2.096(1)	Co1-H2	2	-0.008	0.3078	9.48E-02	2.970	2.699
V_{sphere} (err)[Å ³]	Co1-P1	1	0.002	0.3078	9.48E-02	2.797	2.797
38.55(2)	Co1-P2	2	0.002	0.3078	9.48E-02	3.209	3.209
R-factor	Co1-O3	2	0.001	0.2301	5.29E-02	3.313	3.281
0.008	Co1-P3	1	0.002	0.3078	9.48E-02	3.305	3.305
S_o^2 Amplitude reduction factor	Co1-O4	2	0.001	-0.0171	2.94E-04	3.592	3.560
0.79(6)	Co1-Co2	7	0.010	0.3774	1.42E-01	3.712	3.653
ΔE	Co1-O5	1	0.001	-0.0171	2.94E-04	3.753	3.721
2.6(6)	Co1-N1	1	-0.008	0.3774	1.42E-01	4.010	3.740
	Co1-O6	3	0.001	0.2301	5.29E-02	3.813	3.781
	Co1-O7	1	0.001	0.2301	5.29E-02	3.944	3.912

Table S8: ARTEMIS fit parameter for Co-phosphate octahydrate (CPO), R-factor= 0.005.

sample	scattering path	degeneracy	σ^2	R_{diff} [Å]	R_{diff}^2 [Å ²]	R_{model} [Å]	R_{fit} [Å]
Co-octahydrate	Co1-O1	5	0.011	-0.003	8.53E-06	2.021	2.099
Co₃(PO₄)₂•8H₂O	Co1-O2	1	0.011	-0.003	8.53E-06	2.158	2.155
mean R_{fit} (err) [Å]	Co1-H1	16	0.018	-0.079	6.19E-03	2.451	2.372
2.11(2)	Co1-O2-H2	8	0.001	0.416	1.73E-01	2.593	2.593
V_{sphere} (err)[Å ³]	Co1-H3	4	0.018	-0.079	6.19E-03	3.226	3.147
39.3(6)	Co1-P1	2	0.010	-0.003	9.18E-06	3.194	3.191
R-factor	Co1-H3	8	0.018	-0.079	6.19E-03	3.319	3.240
0.005	Co1-O3	4	0.001	0.416	1.73E-01	3.579	3.389
S_o^2 Amplitude reduction factor (err)	Co1-O1-O2	8	-0.013	0.099	9.82E-03	3.553	3.553
1.3(1)	Co1-O5	2	0.010	-0.003	9.18E-06	3.675	3.576
ΔE	Co1-O1-O2	8	-0.013	0.099	9.82E-03	3.584	3.584
4.9(7)	Co1-O2-O2	8	0.010	-0.003	9.18E-06	3.684	3.672
	Co1-O1-P1	4	-0.013	0.099	9.82E-03	3.389	3.684
	Co1-O4	8	0.010	-0.003	9.18E-06	3.950	3.947
	Co1-H3-O4	16	0.001	0.416	1.73E-01	4.014	4.014
	Co1-O6-H5	8	0.001	0.416	1.73E-01	4.450	4.450

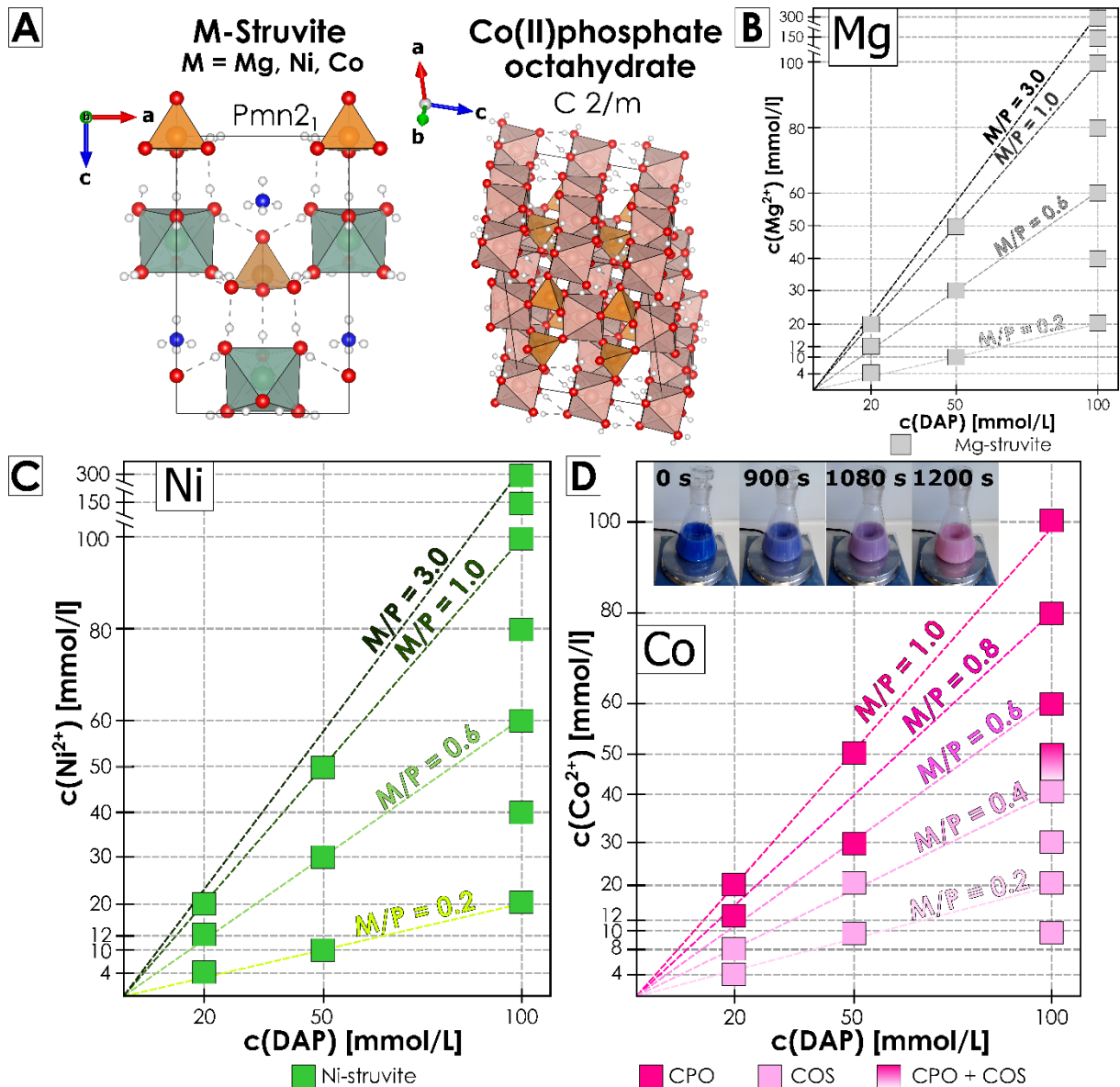


Figure S1: Phase composition diagrams for Mg, Ni, and Co phosphates, which are derived from XRD data (SI: Figures S2-S3); (A) The distinct crystallographic structure of M-struvite $\text{NH}_4\text{MPO}_4 \cdot 6\text{H}_2\text{O}$ (010) plane, M = Mg, Ni, Co and Co(II)phosphate octahydrate $\text{Co}_3(\text{PO}_4)_2 \cdot 8\text{H}_2\text{O}$ is displayed. For (B) Mg and (C) Ni systems, only struvite was observed. For (D) Co a color change of the aqueous solution from blue to purple to light pink at different times can be observed (see inset); The following symbols and abbreviations are used: CPO = $\text{Co}_3(\text{PO}_4)_2 \cdot 8\text{H}_2\text{O}$ cobalt(II)phosphate octahydrate, pakhomovskiyite; COS = $\text{NH}_4\text{CoPO}_4 \cdot 6\text{H}_2\text{O}$ Co-struvite. Crystal structure colors: white = hydrogen H, blue = nitrogen N, red = oxygen O; orange = phosphorous P; turquoise = metal M = Mg, Ni, Co; pink = cobalt Co; dotted lines hydrogen bonds.

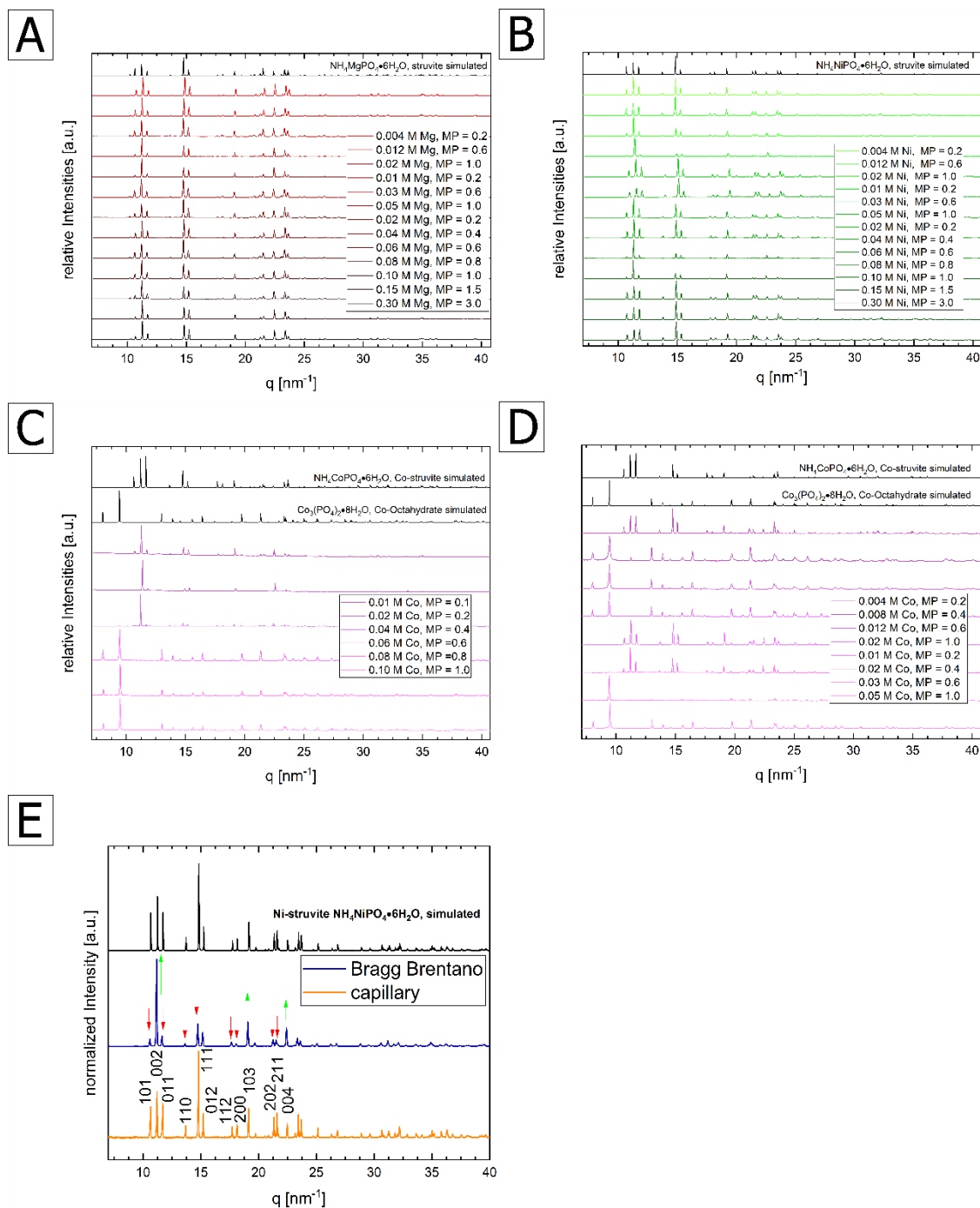


Figure S2: Stacked XRD patterns with the simulated pattern of the phosphate compound in black; (A) Mg-series; (B) Ni-series; (C) and (D) Co-series for different concentrations, according to the legends; These XRD patterns were used to create the phase stability diagrams; Mg-struvite reference COD 9007674; Ni-struvite reference ICSD 403058; Co-struvite reference ICSD 170042; Co(II) phosphate octahydrate reference COD 2020362; (E) In all measured XRD patterns of M-struvite preferred orientation of the (001) crystal planes occurred to a varying degree, and was visible through strong intensity discrepancies between the simulated and measured patterns. All crystal planes with high (h00) or (0k0) component exhibit lower intensities while reflexes with a dominant (00l) component are intensified than in the simulated pattern visible in (E). The preferred orientation is caused by the alignment of elongated habit of the crystals during the preparation of the flat powder sample holders.

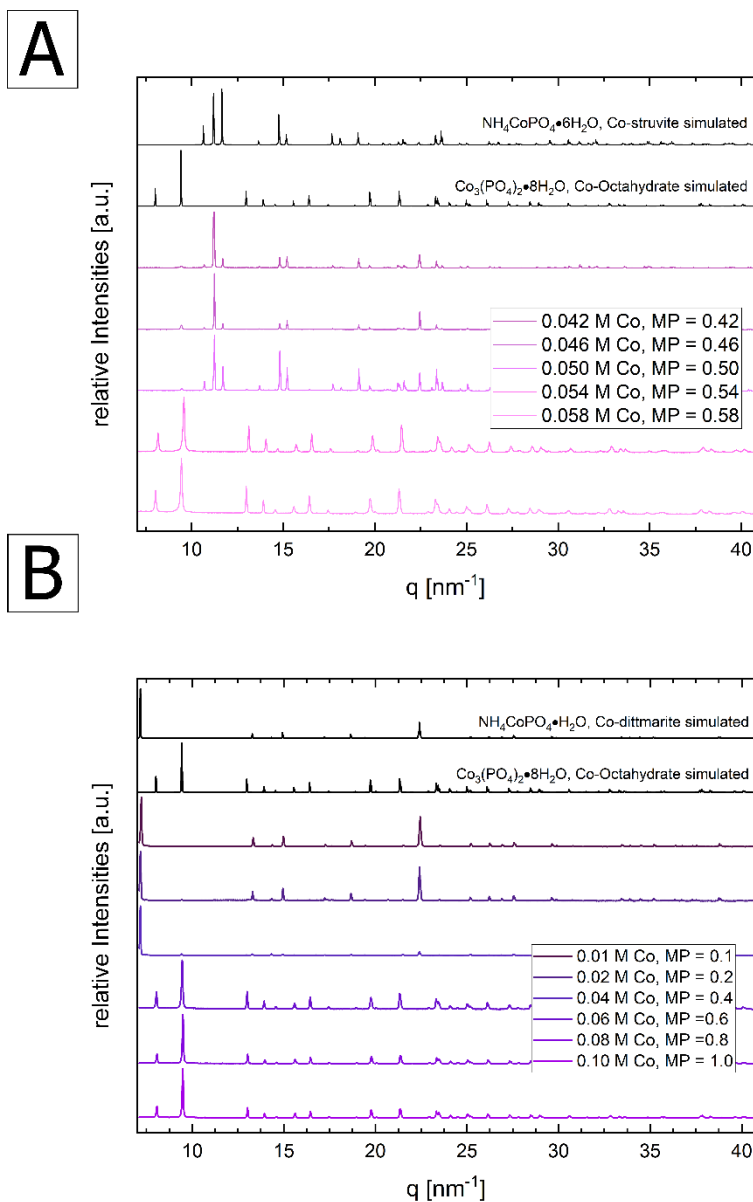


Figure S3: Stacked XRD patterns with the simulated pattern of the phosphate compound in black; (A) In the transition interval between M/P ratios of 0.58-0.42 with 0.1 M DAP of the Co-system Co-struvite and Co(II) phosphate octahydrate are stable; (B) Co-struvite decomposes in air to Co-dittmarite, while Co(II)phosphate octahydrate remains stable under these conditions. The same simulated patterns used as in Figure S2 with added Co-dittmarite COD 2008122.

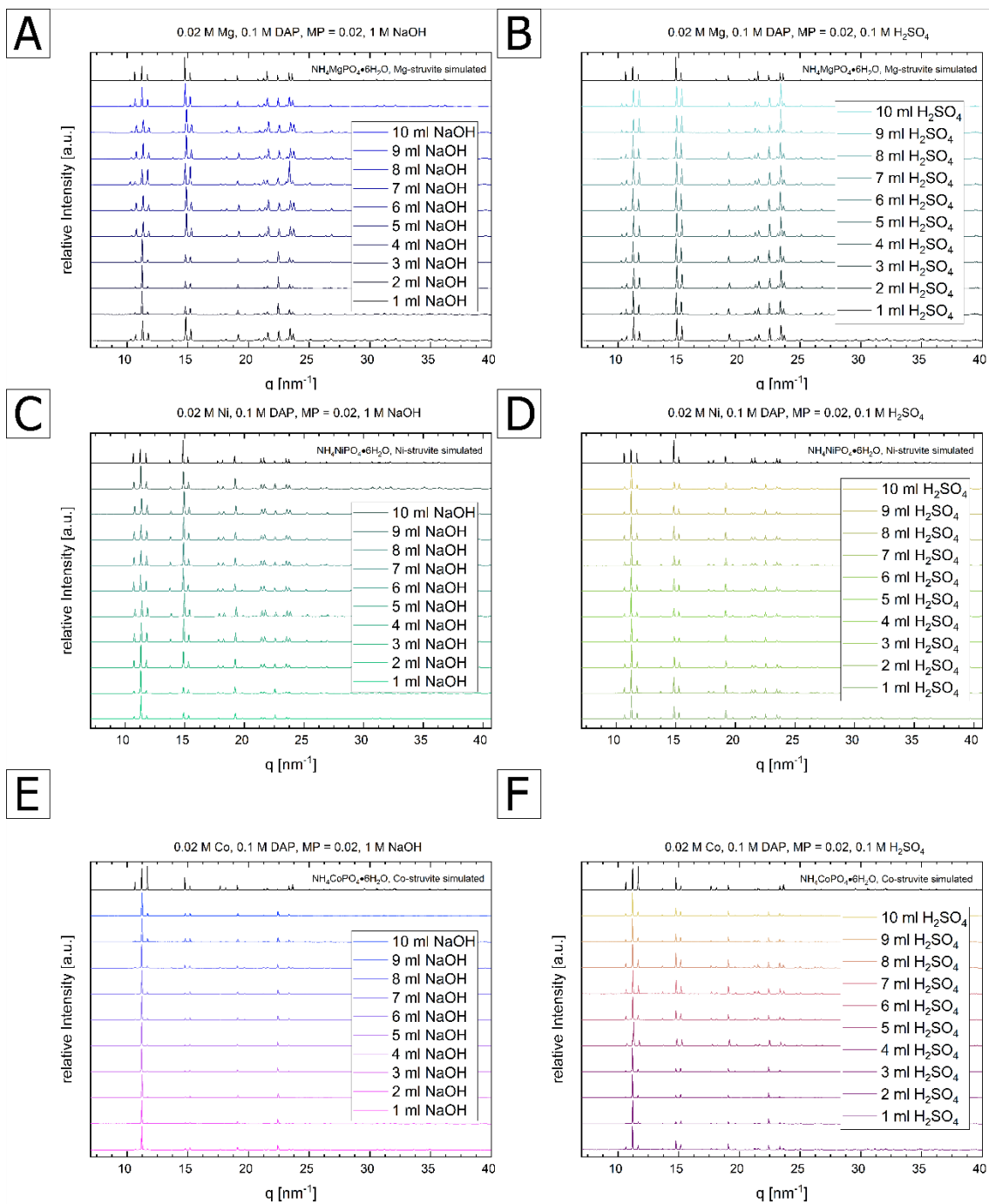


Figure S4: pH adjusted samples with $\text{NaOH}_{(\text{aq})}$ and $\text{H}_2\text{SO}_{4(\text{aq})}$ of (A) (B) Mg; of (C) (D) Ni and (E) (F) Co with their respective experimental conditions (see legends) and their phase composition. In all samples single phase M-struvite precipitated; same simulated patterns used as in Figure S2.

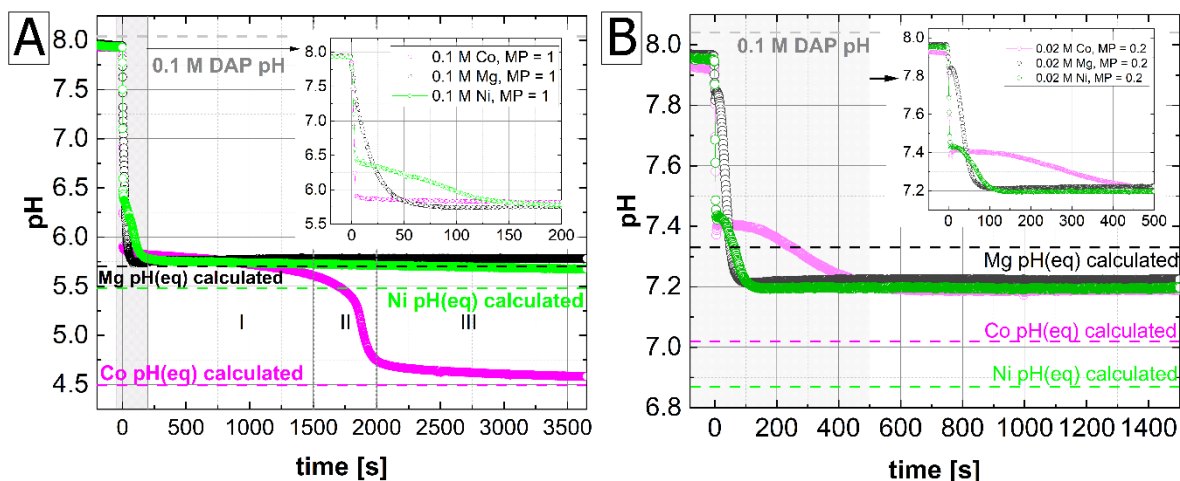


Figure S5: Time-resolved pH measurements with 1 s resolution (A) for the high concentration samples and (B) the low concentration samples; stage I, II, III indicate different slopes in the pH curve of the 0.1 M Co sample; insets show in detail the pH evolution over the first 200 s; the axes and units in the insets are the same as in the main graphs.

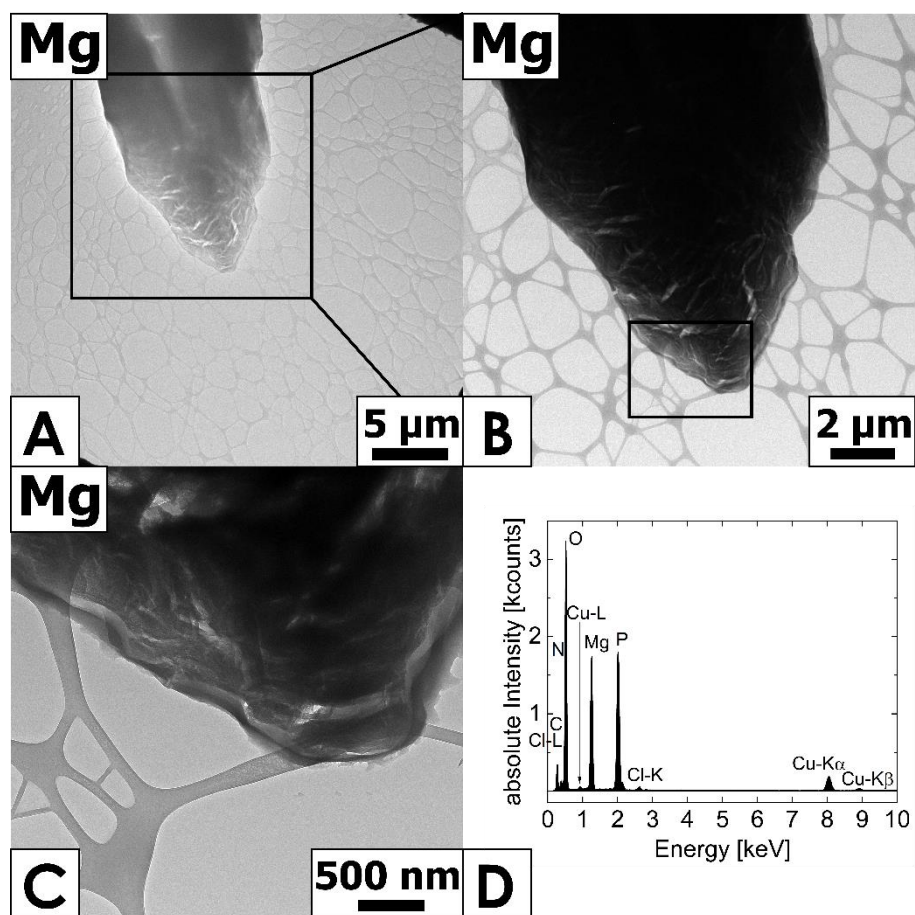


Figure S6: (A) Dry TEM images of Mg sample after 5 seconds mixing forming crystals of μm-size with visible vacuum cracks; (B) detail view of Mg-struvite crystal from the area marked with a black rectangle in (A); (C) close view of the Mg-struvite crystal from the area marked with a black rectangle in (B); (D) EDS spectrum of Mg-struvite.

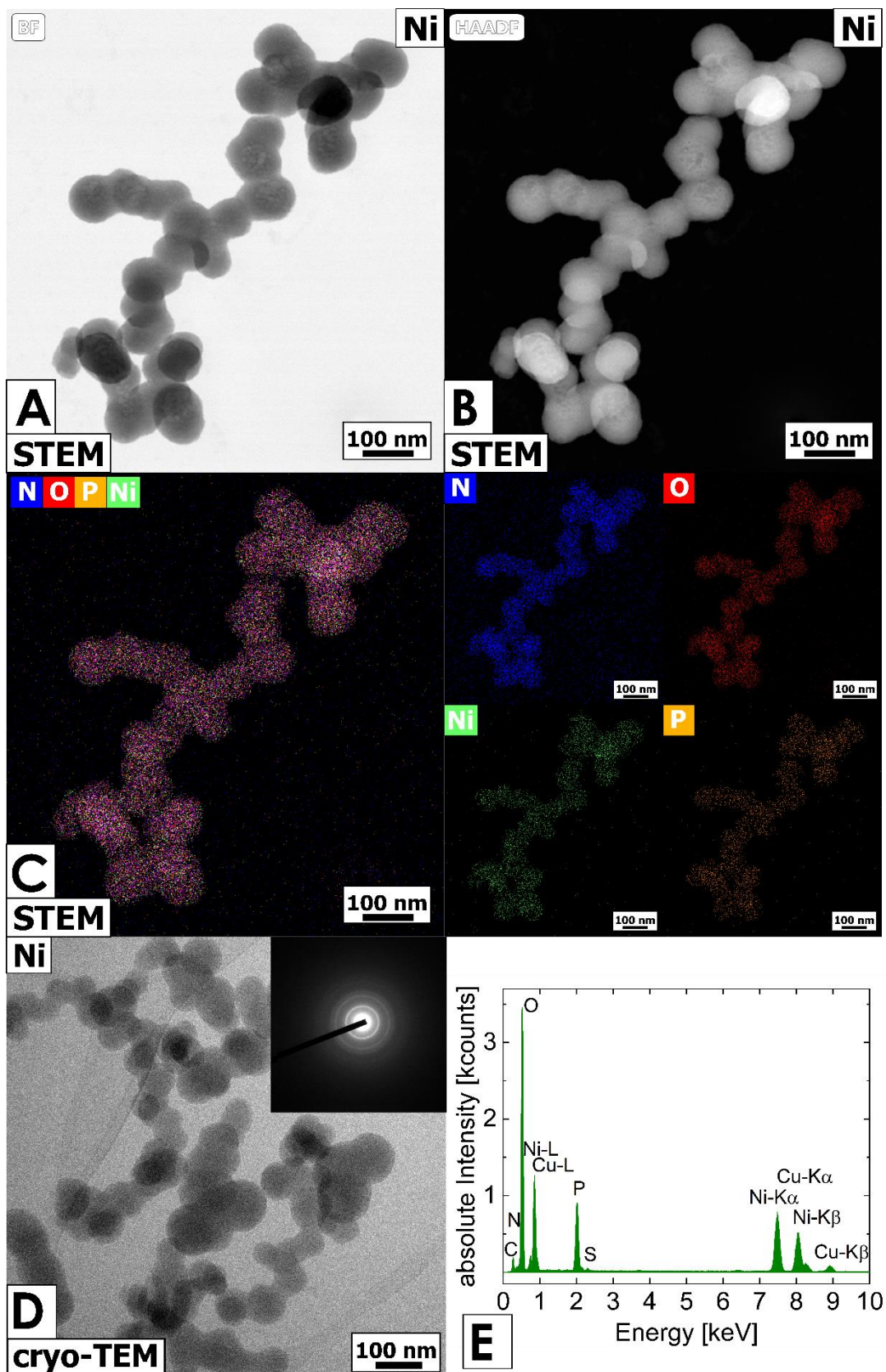


Figure S7: (A) Dry STEM analysis of Ni sample after $t = 5$ sec mixing with the formation of amorphous nanophasers in bright field = BF; (B) high angular dark field = HAADF; (C) and elemental mappings of N = nitrogen, O = oxygen, Ni = nickel and P = phosphorus; (D) cryo-TEM image of amorphous Ni-phase with the SAED pattern in the inset; (E) EDS point measurement from amorphous particles.

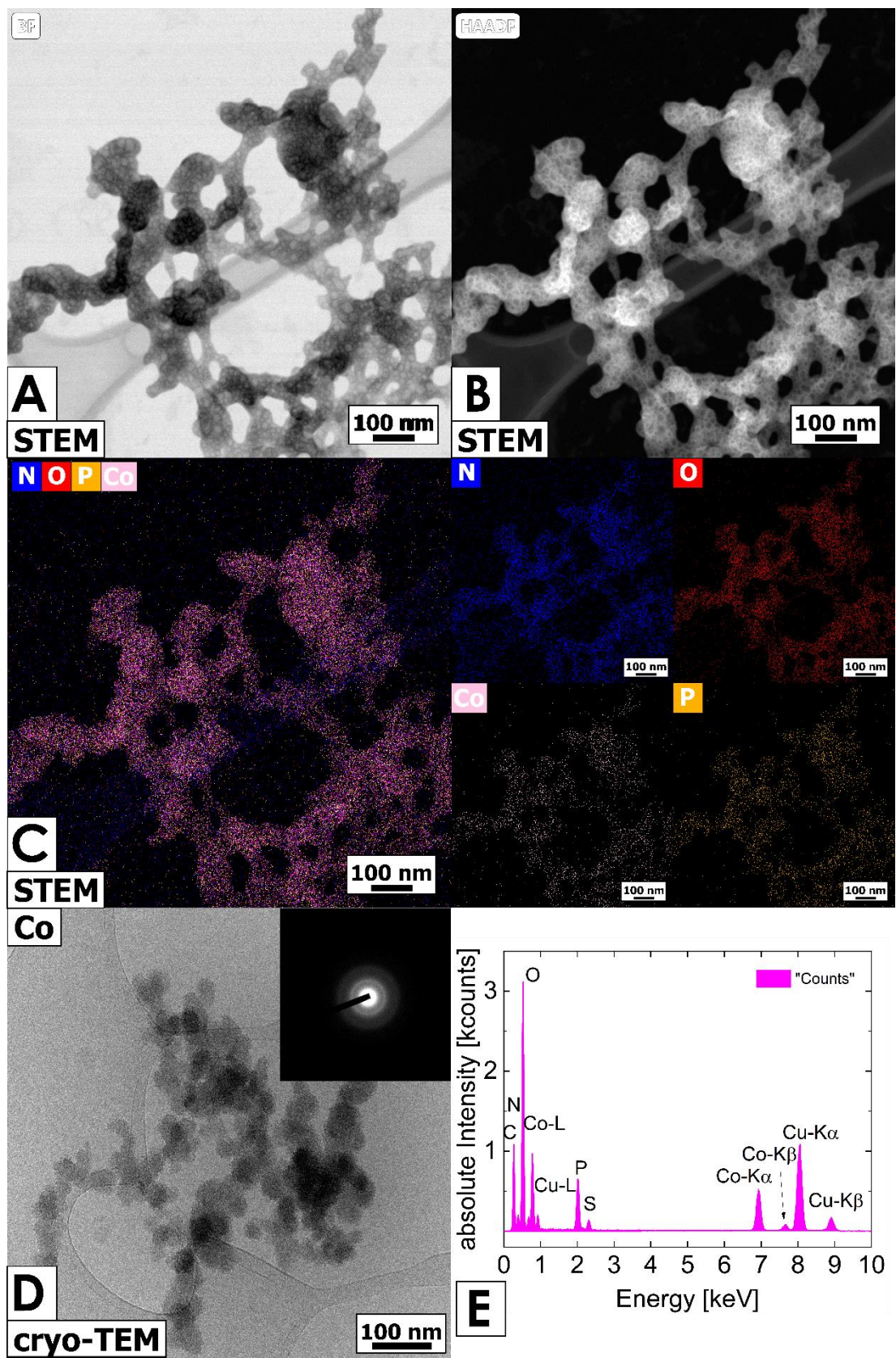


Figure S8: (A) Dry STEM analysis of Co sample after $t = 5$ sec mixing; formation of amorphous nanoparticles in bright field = BF; (B) high angular dark field = HAADF; (C) elemental mappings of N = nitrogen, O = oxygen, Co = cobalt and P = phosphorus; (D) cryo-TEM image of amorphous Co-phase with the SAED pattern; (E) EDS point measurement of amorphous particles.

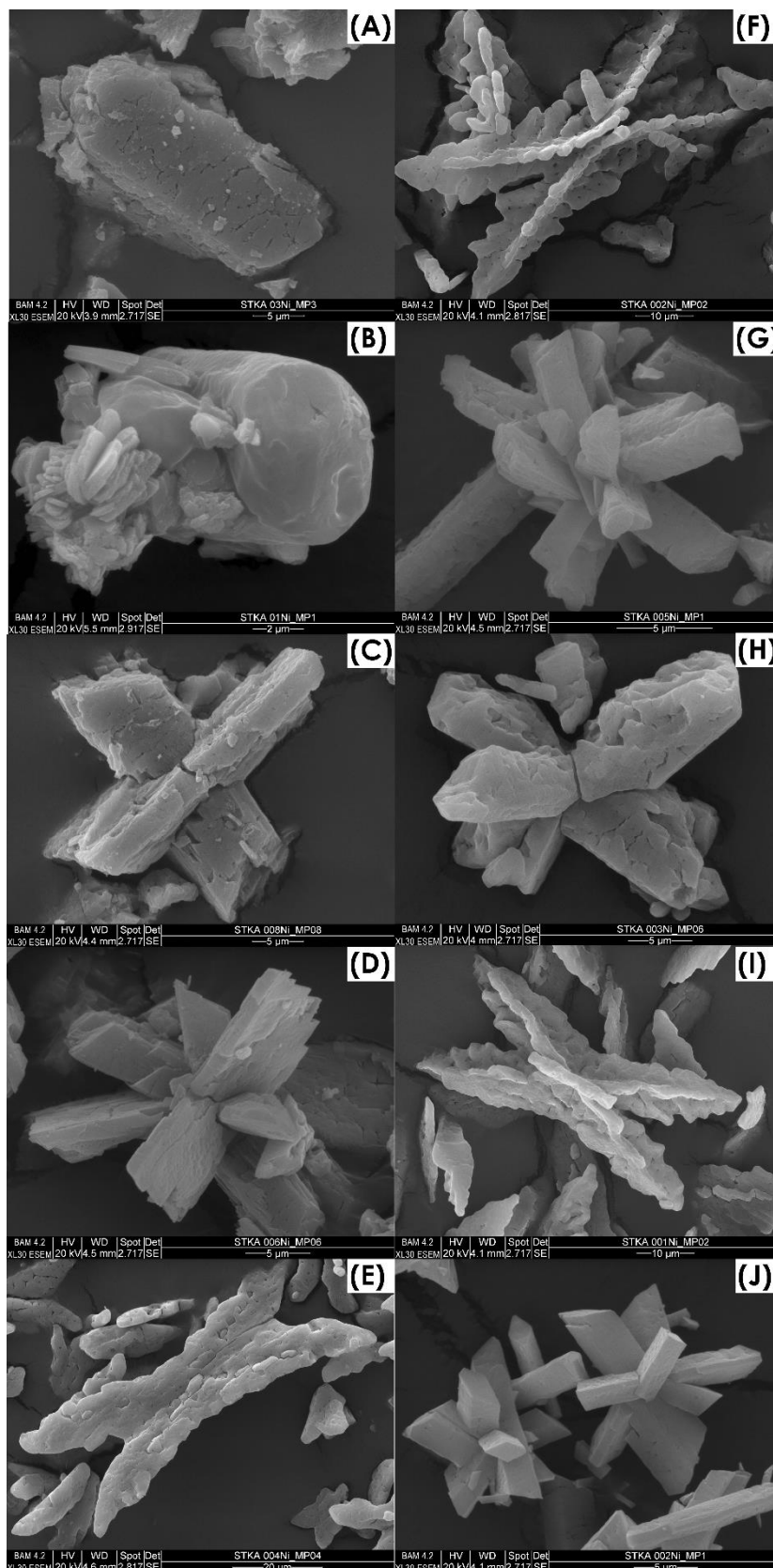


Figure S9: Ni-struvite synthesized at varying concentrations of educts. (A) 0.3 M Ni, 0.1 M DAP, M/P ratio = 3; (B) 0.1 M Ni, 0.1 M DAP, M/P ratio = 1; (C) 0.08 M Ni, 0.1 M DAP, M/P ratio = 0.8; (D) 0.06 M Ni, 0.1 M DAP, M/P ratio = 0.6; (E) 0.04 M Ni, 0.1M DAP, M/P ratio = 0.4; (F) 0.02 M Ni, 0.1 M DAP, M/P ratio = 0.2; (G) 0.05 M Ni, 0.05 M DAP, M/P ratio = 1.0; (H) 0.03 M Ni, 0.05 M DAP, M/P ratio = 0.6; (I) 0.01 M Ni, 0.05M DAP, M/P ratio = 0.2; (J) 0.02 M Ni, 0.02 M DAP, M/P ratio = 1.0.

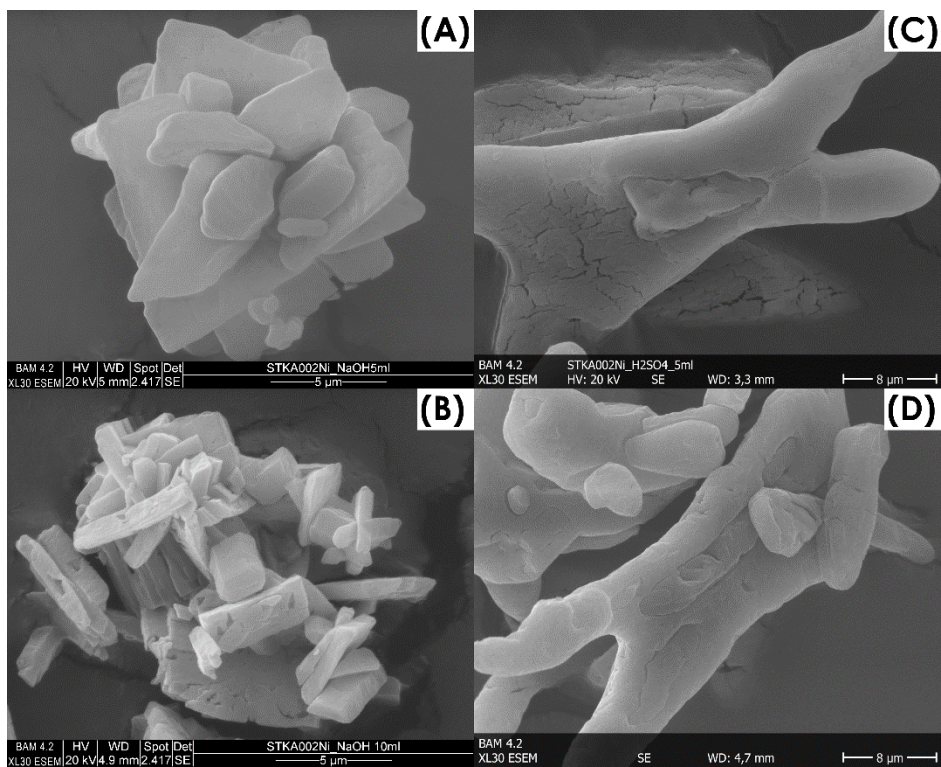


Figure S10: Ni-struvite synthesized from 0.02 M Ni and 0.1 M DAP leading to a M/P ratio of 0.2 at different initial pH with 5 ml and 10 ml 1 M NaOH_(aq) or 0.1 M H₂SO_{4(aq)}; (A) 5 ml 1 M NaOH_(aq); (B) 10 ml 1 M NaOH_(aq); (C) 5 ml 1 M H₂SO_{4(aq)}; (D) 10 ml 1 M H₂SO_{4(aq)}.

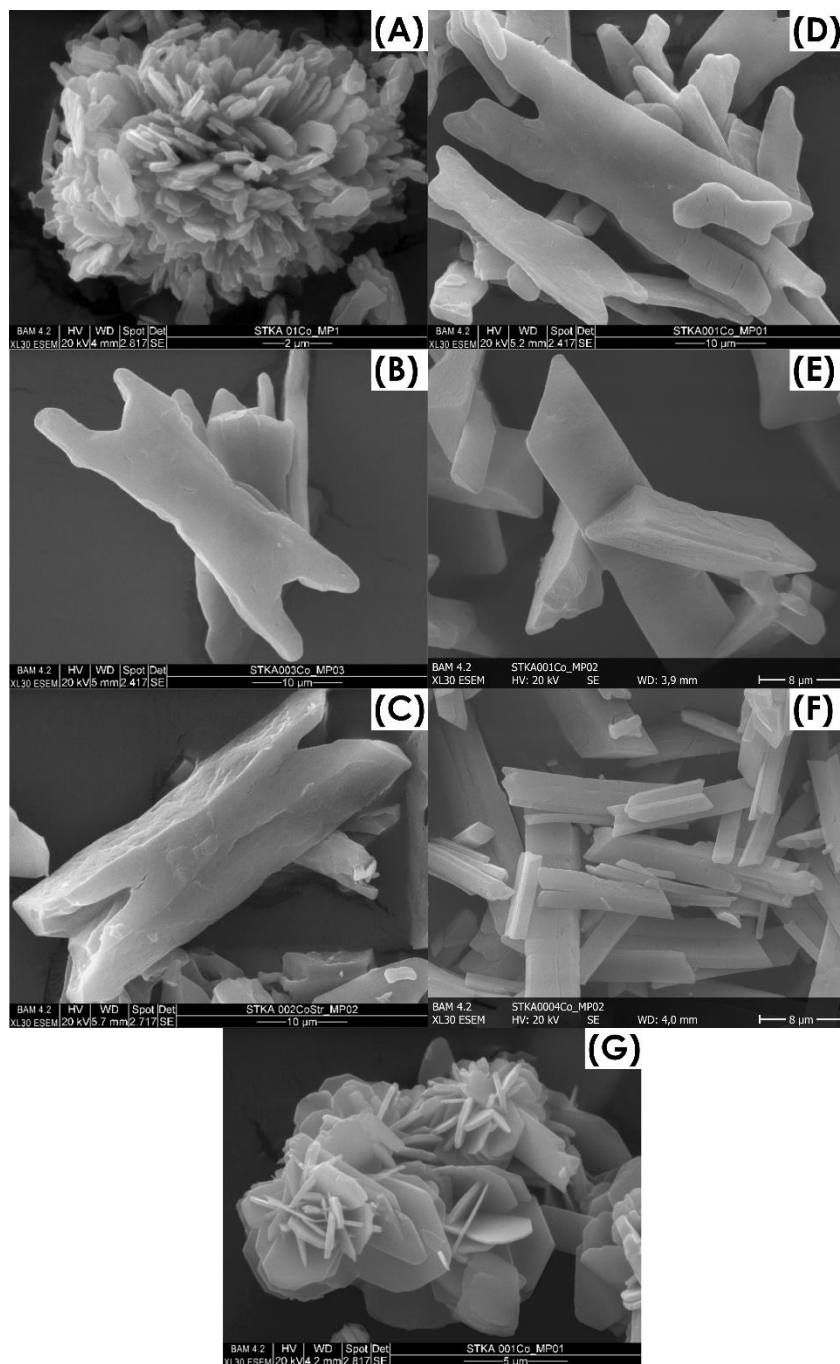


Figure S11: Co-phosphates synthesized at different concentrations. (A) Co(II)phosphate octahydrate 0.1 M Co, 0.1 M DAP, M/P ratio = 1; (B) 0.03 M Co, 0.1 M DAP, M/P ratio = 0.3; (C) 0.02 M Co, 0.1 M DAP, M/P ratio = 0.2; (D) 0.01 M Co, 0.1 M DAP, M/P ratio = 0.1; (E) 0.01 M Co, 0.05 M DAP, M/P ratio = 0.2; (F) 0.004 M Co, 0.02 M DAP, M/P ratio = 0.2; (G) Co-dittmarite in air decomposed 0.01 M Co, 0.1 M DAP, M/P ratio = 1.0.

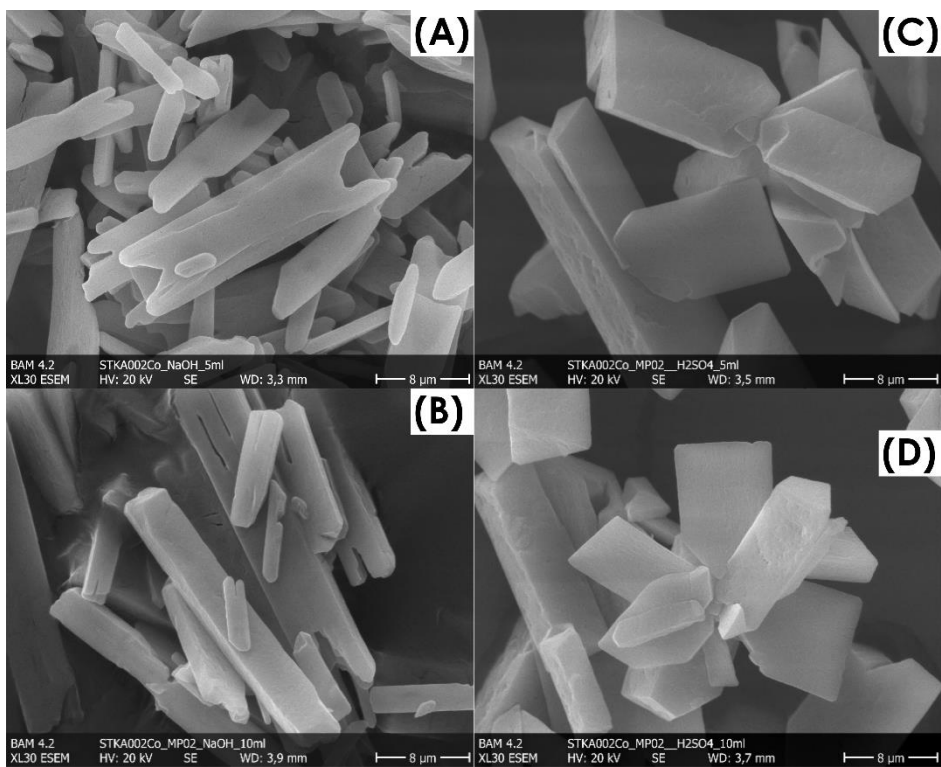


Figure S12: Co-struvite synthesized from 0.02 M Co and 0.1 M DAP leading to a M/P ratio of 0.2 at different initial pH with 5 ml and 10 ml 1 M NaOH_(aq) or 0.1M H₂SO₄(aq); (A) 5 ml 1 M NaOH_(aq); (B) 10 ml 1 M NaOH_(aq); (C) 5 ml 1 M H₂SO₄(aq); (D) 10 ml 1 M H₂SO₄(aq).

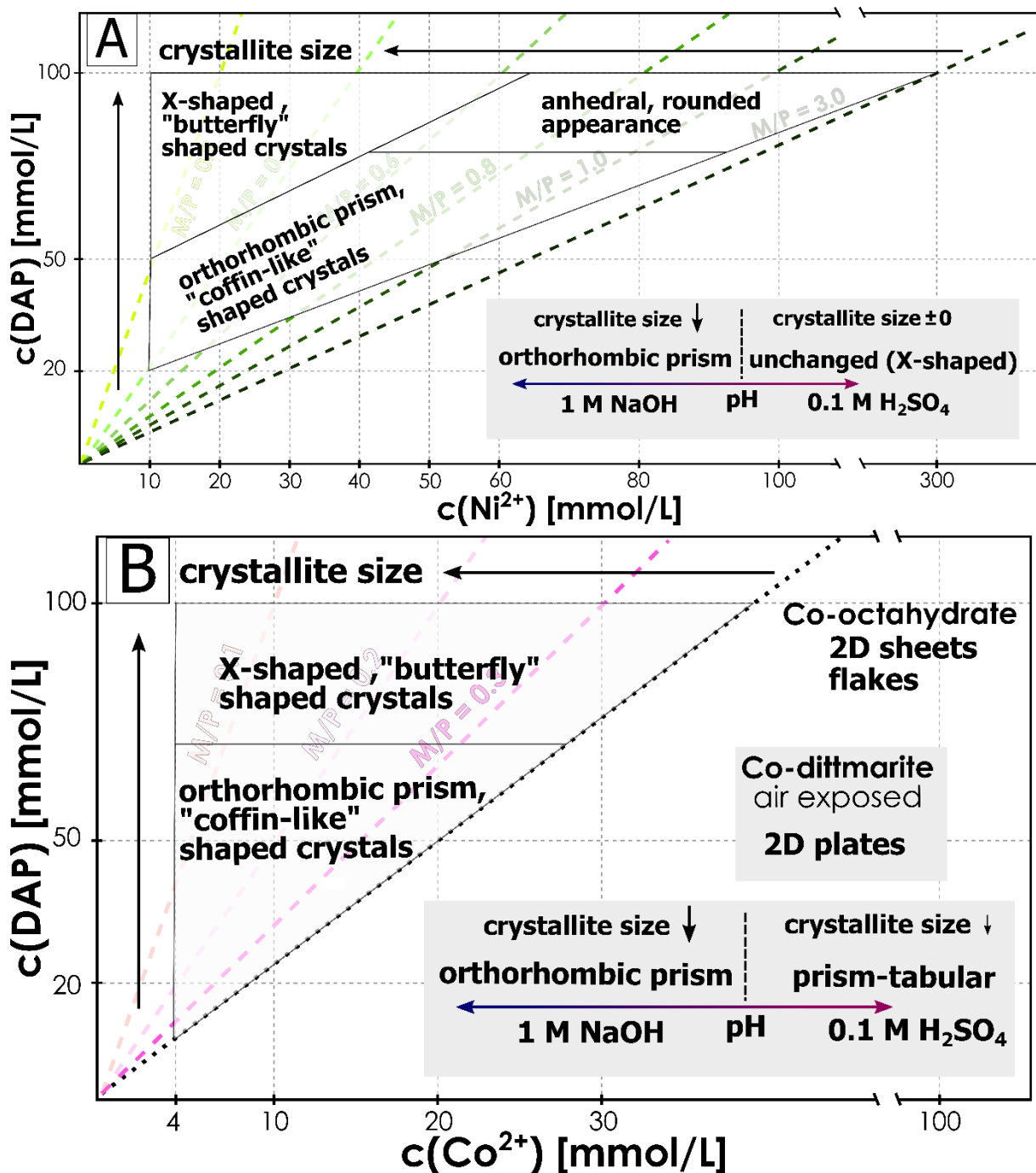


Figure S13: Crystallization trends in the $c(M^{2+})$ vs. $c(DAP)$ plots with (A) green (for Ni) and (B) pink (for Co) dotted lines indicating the distinct M/P ratio of the sample. Crystal morphology fields are displayed in the triangles. The crystallite size increases with higher DAP and lower M^{2+} contents (see direction of the arrows); Adding $NaOH_{(aq)}$ decreased the crystallite size and favored the formation of orthorhombic prisms. Co-octahydrate exhibits a 2D sheet or flake morphology. Co-dittmarite (formed due to air exposure) shows a 2D plate habit. In the Ni-system the crystallite size remained unchanged and while in the Co-system the crystals decreased slightly in size and habit to more tabular-shaped crystals.

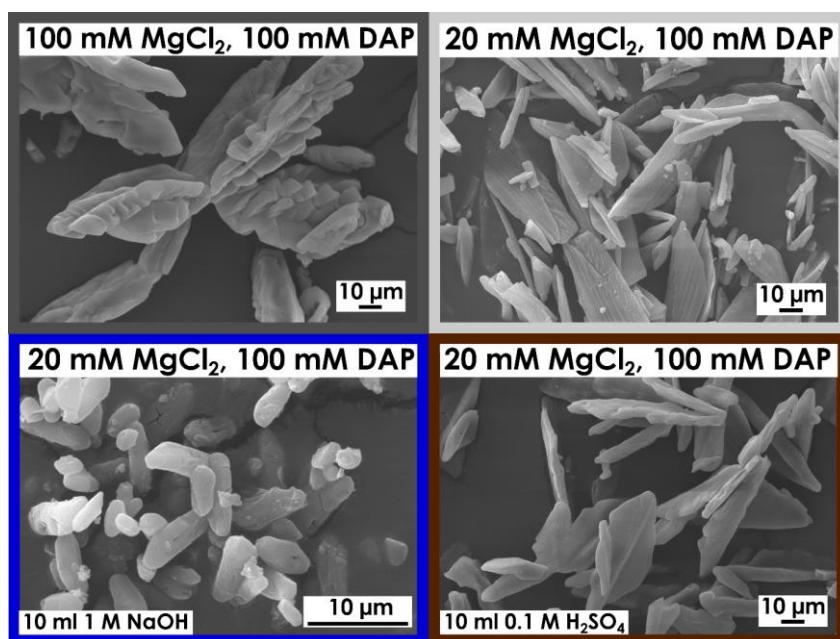


Figure S14: SEM images of different Mg-struvites at low M/P ratios of 0.2 with pH adjusted samples at the sides and one sample with high M/P ratio of 1; frame colors indicate different conditions: dark grey = $c(\text{Mg}^{2+})$ of 0.1 M, light grey = $c(\text{Mg}^{2+})$ of 0.02 M; blue = basic pH conditions of 10 ml 1 M NaOH_(aq); brown = acidic pH conditions with 10 ml 0.1 M H₂SO_{4(aq)}.

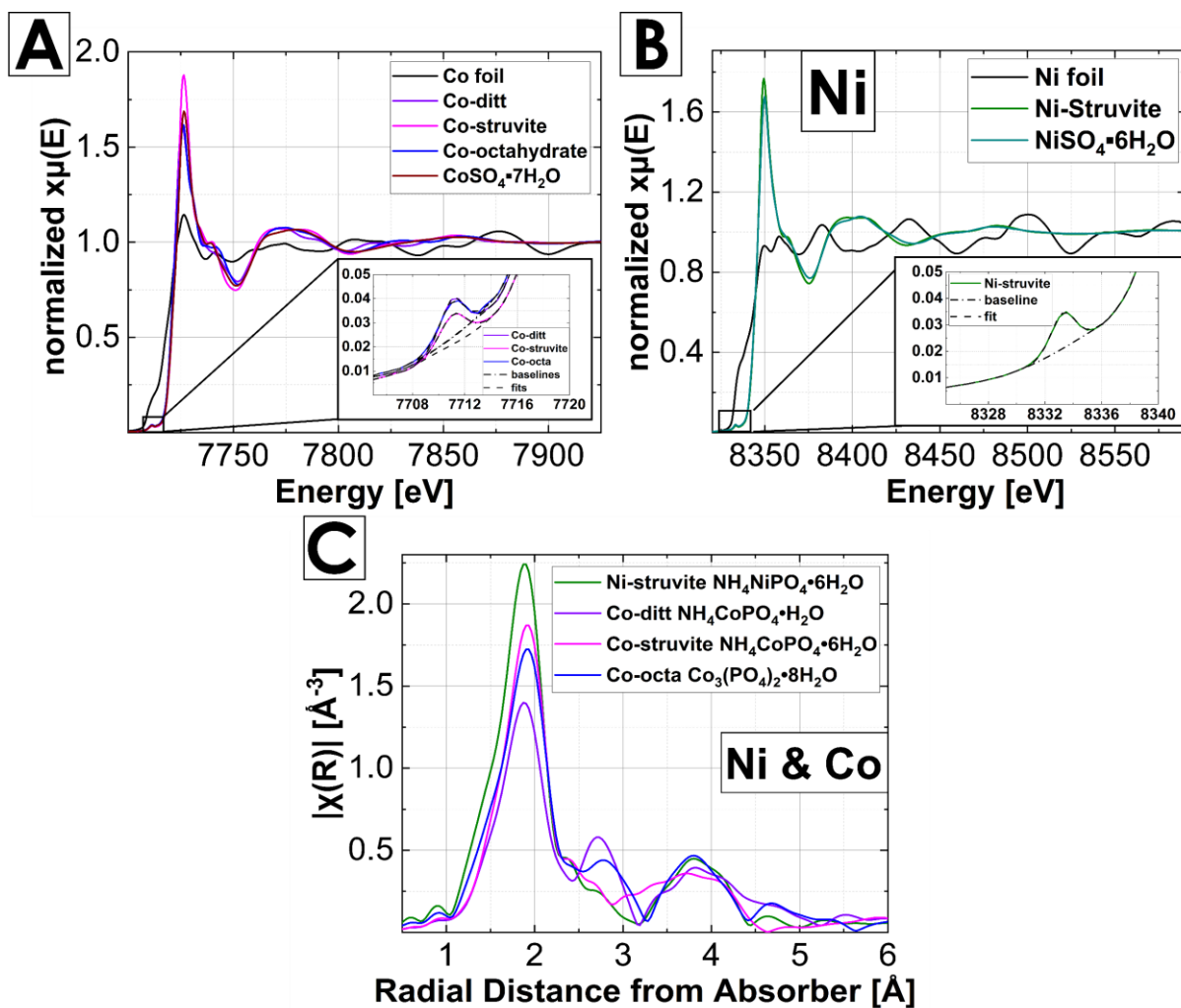


Figure S15: XAS spectra of (A) Co and (B) Ni samples with detailed view of the pre-peak region; (C) Fourier-transformed Ni- and Co spectra plotted in R-space; the axes and units in the insets are the same as in the main graphs.

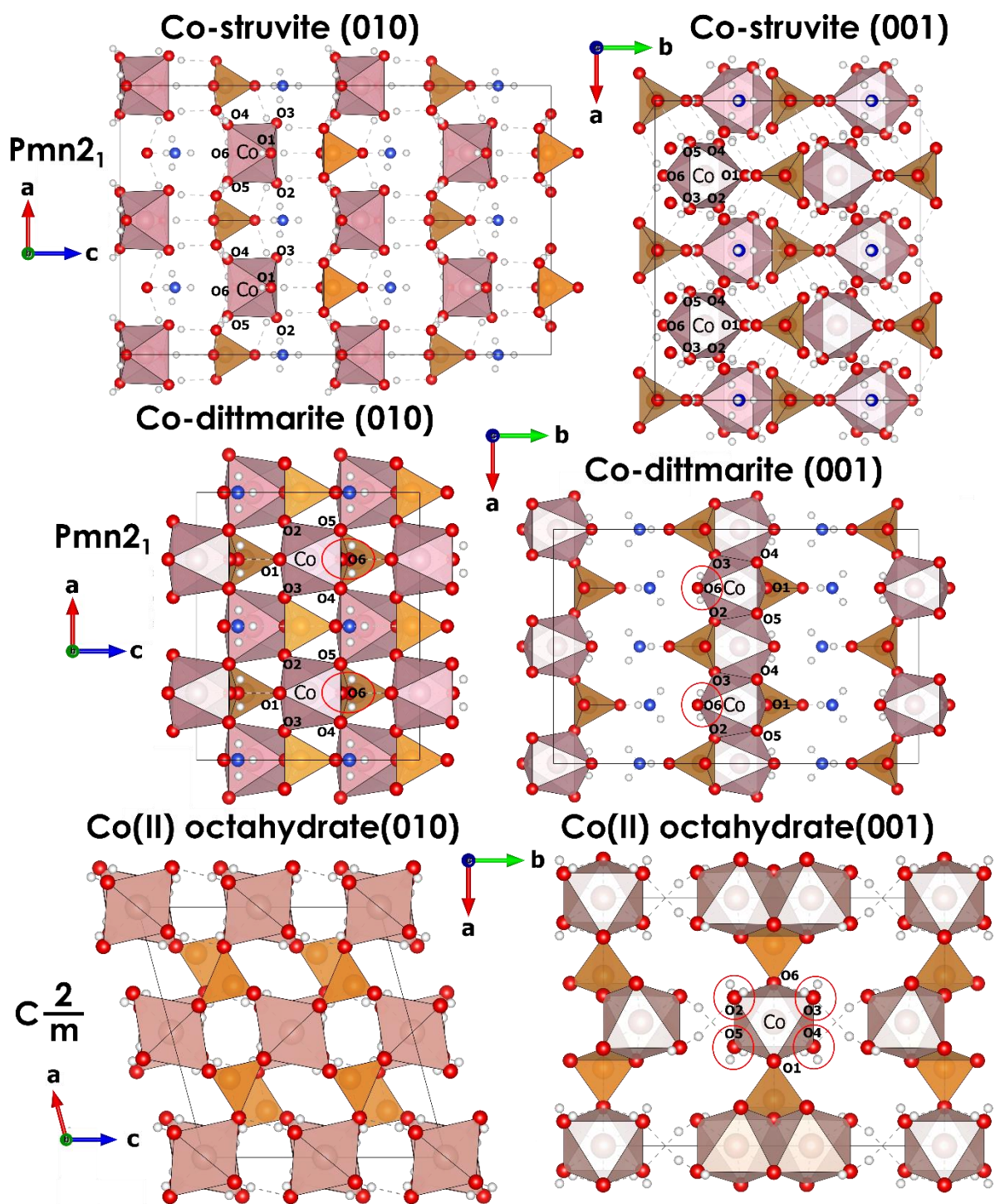


Figure S16: The (010) and (001) crystal planes of Co-struvite $\text{NH}_4\text{CoPO}_4 \cdot 6\text{H}_2\text{O}$, Co-dittmarite $\text{NH}_4\text{CoPO}_4 \cdot \text{H}_2\text{O}$ and Co(II)phosphate octahydrate $\text{Co}_3(\text{PO}_4)_2 \cdot 8\text{H}_2\text{O}$ crystal structure is displayed with the respective space group $\text{Pmn}2_1$ for Co-struvite and Co-dittmarite (orthorhombic) and space group $\text{C}2/m$ (monoclinic); Co: light pink, P: orange, O: red; N: blue and H: white; one or two exemplary CoO_6 octahedrons are marked by atom labels with all the coordinating oxygen numbered; the coordinating crystal water in Co-dittmarite and Co-octahydrate is marked with red ellipsoids; note that in the Co-dittmarite and Co-octahydrate structures, the CoO_6 is linked to the phosphate tetrahedrons, while in the Co-struvite structure the CoO_6 is isolated by six coordinating crystal water oxygens.

Supplementary Note 1

Cobalt is classified as a CRM according to the EU, because it is used in a number of technological applications, but it is only exploitable in few ore deposits in the world, mostly located in the Democratic Republic of the Congo. There, it is concentrated in minerals such as the cobaltite (CoAsS), erythrite ($\text{Co}_3(\text{AsO}_4)_2 \cdot 8\text{H}_2\text{O}$) or skutterudite (CoAs_3) in hydrothermal altered mantle rocks in association with mainly nickel. Although, it also plays an essential role in several enzymes and co-enzymes involved in the metabolism of animals and plants for example vitamin B12 (cobalamin), at above-trace concentrations cobalt is highly toxic.

Nickel is widely used in the industry and is also relatively common. It is mined in lateritic ultramafic rocks from ore minerals like pentlandite ($(\text{Ni,Fe})_8\text{S}_9$) or nickel ferrous limonite ($(\text{Ni,Fe})\text{O}(\text{OH})$). Unfortunately, in the environment nickel compounds cause numerous carcinogenic effects in human and plants and it is one of the most common allergens in the world. This is even though at trace concentrations it also plays an important biological role for plants and microbes as a part of enzymes such as urease^{11,12}. Hence although nickel is not a CRM, it should be recovered from wastewater.

In mining waters of the Eshidiya mine (Jordan) the PO_4^{3-} and NH_4^+ content ranges from 0.1 - 8.9 mg/l and 0.03 - 0.95 mg/l, respectively⁵. The related ground water in the same region showed concentrations values of PO_4^{3-} and NH_4^+ at 3.5-3.8 and 0.01-0.05 mg/l. Mine wastewaters from the Duluth Gabbro complex in Minnesota (USA) contain average values of 198 mg/l of Ni and 9.8 mg/l of Co⁴. In the Katanga province (DRC) in effluent surface mine waters of a Co-Cu ore deposit Co reached maximum concentrations of 3.16 mg/l¹. In Rio Piscianas (Italy) the highly contaminated groundwater from mining activities in the 1990s had concentrations of 1.5-2.9 mg/l for Co and 3.0-4.6 mg/l for Ni². Ground water samples from the Amik plain (Turkey) contain in average 13 mg/l NH_4^+ , 87 mg/l Phosphorus, 13 $\mu\text{g/l}$ Co and 50 $\mu\text{g/l}$ Ni³.

These numbers prove that transition metals as well as ammonia and phosphate are common contaminants in ground and wastewaters (Table S3). As mining wastewaters contain high amounts of transition metals (mg/l) at low pH (~4-5) while agricultural waste- and ground waters demonstrate high concentrations of phosphate and ammonium at medium to high pH (7-9) a mixture of both wastewaters could lead to precipitation of M-struvite in significant amounts. By mixing different wastewaters together multiple environmental critical compounds could be extracted simultaneously. Further experiments to the up scalability and implementation as wastewater treatment method would quantitatively evaluate if the precipitation of M-struvite is applicable as wastewater treatment method or not.

Supplementary Note 2

The initial pH was ~ 7.9 for the 0.1 M DAP solution and ~ 5.7 for both NiSO_4 and CoSO_4 solutions at 0.1 M, and the 0.1 M MgCl_2 solution exhibited an initial pH of 7.0. When metal salt and DAP equimolar solutions were mixed, near-instant precipitation could be observed in both transition metal systems with the simultaneous drop in pH. On the other hand, the Mg-system had exhibited an induction time of ~ 5 s before it turned turbid. Immediately after mixing both 0.1 M solutions the pH dropped down to around ~ 5.8 for all systems. While the pH of the 0.1 M Mg and Ni sample declined slightly over the first 50 - 150 s with different slopes to a stable plateau value of 5.8, the pH for 0.1 M Co reached nearly instantaneously a plateau value of 5.9 and was only slightly until around 1500 s, marked by phase I (SI: Figure S5). After 1500 s a significant pH jump to a value of 4.6 over 500 s occurred in the 0.1 M Co sample marked by phases II and III which was most likely related to the transformation of the colloidal phases as the color changed simultaneously from purple to light pink.

The initial pH of the 0.02 M metal solutions was 6.5 (Mg), 5.9 (Ni and Co) for the low concentration runs. The same 0.1 M DAP solution was used as before. Similar trends as in the highly concentrated equimolar solution runs were observed except for Co although in all systems M-struvite formed. In this case, the pH of the Co mixture declined slowly after 450 s to 7.2 and stagnated at this value, as was the case for the other struvite samples. The PHREEQC equilibrium pH calculations are in a relatively close agreement with the experimental values within a confidence interval of $\Delta\text{pH} \approx 0.3$ (colored dotted lines in Figure S5). That indicates a progression of the precipitation reaction to completion for all the samples. The deviation between the calculated and measured pH trends, occurred probably due to the presence of amorphous phases, which were difficult to consider in the calculations as barely any (if any) thermodynamic data exist for them.

The Ni- and Mg-struvite formation reaction proceeds fast within the first 100 - 150 s, while the Co-phosphate reactions exhibit much longer reaction times (400 s for 0.02 M and around 3000 s for 0.1 M Co^{2+}) due to the preservation and transformation of long-lived colloidal phases.

References SI

1. Atibu, E. K.; Devarajan, N.; Thevenon, F.; Mwanamoki, P. M.; Tshibanda, J. B.; Mpiana, P. T.; Prabakar, K.; Mubedi, J. I.; Wildi, W.; Poté, J., Concentration of metals in surface water and sediment of Luilu and Musonoie Rivers, Kolwezi-Katanga, Democratic Republic of Congo. *Applied Geochemistry* **2013**, *39*, 26-32.
2. Concas, A.; Arda, C.; Cristini, A.; Zuddas, P.; Cao, G., Mobility of heavy metals from tailings to stream waters in a mining activity contaminated site. *Chemosphere* **2006**, *63*, (2), 244-53.
3. Agca, N.; Karanlik, S.; Odemis, B., Assessment of ammonium, nitrate, phosphate, and heavy metal pollution in groundwater from Amik Plain, southern Turkey. *Environ Monit Assess* **2014**, *186*, (9), 5921-34.
4. Hammack, R.; Edenborn, H., the removal of nickel from mine waters using bacterial sulfate reduction. *Proceedings American Society of Mining and Reclamation* **1991**, 97-108.
5. Al-Hwaiti, M. S.; Brumsack, H. J.; Schnetger, B., Suitability assessment of phosphate mine waste water for agricultural irrigation: an example from Eshidiya Mines, South Jordan. *Environmental Earth Sciences* **2016**, *75*, (3).
6. Sracek, O.; Mihaljevič, M.; Křibek, B.; Majer, V.; Veselovský, F., Geochemistry and mineralogy of Cu and Co in mine tailings at the Copperbelt, Zambia. *Journal of African Earth Sciences* **2010**, *57*, (1-2), 14-30.
7. Feng, C.; Zhang, S.; Wang, Y.; Wang, G.; Pan, X.; Zhong, Q.; Xu, X.; Luo, L.; Long, L.; Yao, P., Synchronous removal of ammonium and phosphate from swine wastewater by two agricultural waste based adsorbents: Performance and mechanisms. *Bioresour Technol* **2020**, *307*, 123231.
8. Leite, V.; Athayde Junior, G.; Sousa, J.; Lopes, W.; Henrique, I., Treatment of Domestic Wastewater in Shallow Waste Stabilization Ponds for Agricultural Irrigation Reuse. *Journal of Urban and Environmental Engineering* **2009**, *3*, (2), 58-62.
9. Percival, J.; Dumaresq, C.; Kwong, Y.; Hendry, K.; Michel, F., Arsenic in surface waters, Cobalt, Ontario. *Current Reserach 1996-C* **1996**, 137-146.
10. Stopic, S.; Pavlovic, J.; Friedrich, B., treatment of Highly Contaminated Waste Waters in a Continous Cascade Line Reactor. *World of metallurgy - ERZMETALL* **2007**, *60*, 255-262.
11. Carter, E. L.; Flugga, N.; Boer, J. L.; Mulrooney, S. B.; Hausinger, R. P., Interplay of metal ions and urease. *Metallomics* **2009**, *1*, (3), 207-21.
12. Mazzei, L.; Musiani, F.; Ciurli, S., The structure-based reaction mechanism of urease, a nickel dependent enzyme: tale of a long debate. *J Biol Inorg Chem* **2020**, *25*, (6), 829-845.